

Large-Scale Meteorology and Deep Convection during TRMM KWAJEX*

ADAM H. SOBEL

*Department of Applied Physics and Applied Mathematics, and Department of Earth and Environmental Sciences, Columbia University,
New York, New York*

SANDRA E. YUTER AND CHRISTOPHER S. BRETHERTON

Department of Atmospheric Sciences, University of Washington, Seattle, Washington

GEORGE N. KILADIS

NOAA/Aeronomy Laboratory, Boulder, Colorado

(Manuscript received 9 January 2003, in final form 7 July 2003)

ABSTRACT

An overview of the large-scale behavior of the atmosphere during the Tropical Rainfall Measuring Mission (TRMM) Kwajalein Experiment (KWAJEX) is presented. Sounding and ground radar data collected during KWAJEX, and several routinely available datasets including the Geostationary Meteorological Satellite (GMS), NOAA outgoing longwave radiation (OLR), the Special Sensor Microwave Imager (SSM/I), and ECMWF operational analyses are used. One focus is on the dynamical characterization of synoptic-scale systems in the western/central tropical Pacific during KWAJEX, particularly those that produced the largest rainfall at Kwajalein. Another is the local relationships observed on daily time scales among various thermodynamic variables and areal average rain rate. These relationships provide evidence regarding the degree and kind of local thermodynamic control of convection.

Although convection in the Marshall Islands and surrounding regions often appears chaotic when viewed in satellite imagery, the largest rain events at Kwajalein during the experiment were clearly associated with large-scale envelopes of convection, which propagated coherently over several days and thousands of kilometers, had clear signals in the lower-level large-scale wind field, and are classifiable in terms of known wave modes. Spectral filtering identifies mixed Rossby-gravity (MRG) and Kelvin waves prominently in the OLR data. "Tropical depression-type" disturbances are also evident. In some cases multiple wave types may be associated with a single event. Three brief case studies involving different wave types are presented.

Daily-mean sounding data averaged over the five sounding sites show evidence of shallow convective adjustment, in that near-surface moist static energy variations correlate closely with lower-tropospheric temperature. Evidence of thermodynamic control of deep convection on daily time scales is weaker. Upper-tropospheric temperature is weakly correlated with near-surface moist static energy. There are correlations of relative humidity (RH) with deep convection. Significant area-averaged rainfall occurs only above a lower-tropospheric RH threshold of near 80%. Above this threshold there is a weak but significant correlation of further lower-tropospheric RH increases with enhanced rain rate. Upper-tropospheric RH increases more consistently with rain rate. Lag correlations suggest that higher lower-tropospheric RH favors subsequent convection while higher upper-tropospheric RH is a result of previous or current convection. Convective available potential energy and surface wind speed have weak negative and positive relationships to rain rate, respectively. A strong relationship between surface wind speed (a proxy for latent heat flux) and rain rate has been recently observed in the eastern Pacific. It is suggested that in the KWAJEX region, this relationship is weaker because there are strong zonal gradients of vertically integrated water vapor. The strongest surface winds tend to be easterlies, so that strong surface fluxes are accompanied by strong dry-air advection from the east of Kwajalein. These two effects are of opposite sign in the moist static energy budget, reducing the tendency for strong surface fluxes to promote rainfall.

* Supplemental information related to this paper is available at the Journals Online Web site: <http://dx.doi.org/10.1175/MWR2656sup11>.

Corresponding author address: Adam H. Sobel, Dept. of Applied Physics and Applied Mathematics, Columbia University, 500 West 120th St., Rm. 217, New York, NY 10027.
E-mail: ahs129@columbia.edu

1. Introduction

The Kwajalein Experiment (KWAJEX) was one of several field campaigns carried out as part of the National Aeronautics and Space Administration's (NASA) Tropical Rainfall Measuring Mission (TRMM) ground validation program (Kummerow et al. 2000). Centered on Kwajalein Atoll in the Republic of the Marshall Islands, KWAJEX was unique among these campaigns as it was the only one conducted over the tropical open ocean. During the period 23 July–15 September 1999 coordinated datasets were obtained by three aircraft, five upper-air sounding sites, and remote and in situ surface-based sensors on islands, buoys, and the National Oceanic and Atmospheric Administration (NOAA) ship *Ronald H. Brown* (Yuter et al. 2003, manuscript submitted to *J. Appl. Meteor.*, hereafter YUT).

The primary goal of KWAJEX was to obtain data that could be used to evaluate and refine some of the key physical assumptions employed in the TRMM satellite precipitation retrieval algorithms. As such, the observational strategy of KWAJEX focused predominantly on measurement of relatively small-scale variability of parameters within precipitating clouds. Nonetheless, by virtue of the substantial augmentation of the routine observational network that occurred around Kwajalein during the experiment, the KWAJEX data provide an opportunity to investigate the large-scale meteorology of the KWAJEX region and its relation to convective activity. This study is a first step toward using the KWAJEX data to address some outstanding questions in the large-scale atmospheric dynamics of the KWAJEX region and, to some degree, the Tropics in general.

In addition to the inherent scientific motivation behind such a study, we aim to provide large-scale context for other studies using the KWAJEX data, many of which will presumably focus on cloud microphysics and other issues of more direct relevance to the TRMM satellite retrievals. To this end, some of this study (particularly sections 3a and 3c) is descriptive and taxonomic, aiming to provide a succinct depiction and categorization of meteorological events. While we formulate some hypotheses regarding mechanisms behind those events, we do not attempt to test those hypotheses rigorously here. Such testing will require either numerical modeling or statistical analyses applied to observational data from longer time periods. Here, we limit ourselves solely to data obtained during the KWAJEX period.

The issues we address are 1) what were the dominant modes of large-scale meteorological variability during KWAJEX? 2) How were the most significant precipitation events during KWAJEX related to those modes of large-scale variability? 3) Do the KWAJEX observations shed any light on what factors control the occurrence of deep convection over the tropical oceans?

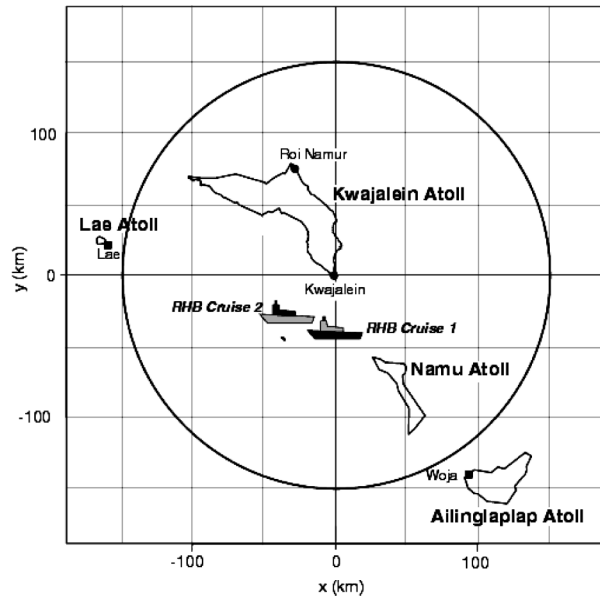


FIG. 1. Map showing the KWAJEX study area, including rawinsonde sites on the R/V *Ronald H. Brown* (RHB) and at Kwajalein, Lae, Roi-Namur, and Woja on the edges of largely submerged coral atolls. A 150-km-range circle around the Kwajalein ground-validation radar encompasses the region over which our radar-based precipitation estimates are taken. The latitude and longitude of Kwajalein are 8.72°N , 167.73°E .

2. Data

a. Soundings

Upper-air soundings were obtained from five locations in the KWAJEX domain (Fig. 1): the islands of Roi-Namur, Kwajalein, Lae, and Woja, and the NOAA ship *Ronald H. Brown* (YUT). For reference, the latitude and longitude of Kwajalein Island are 8.72°N , 167.73°E . Sounding launch frequency varied depending on meteorological conditions and aircraft mission status with the highest frequency (every 3 h) prior to and during major precipitation events and the lowest frequency (every 12 h) during quiescent periods. Three different types of sounding equipment were utilized, non-GPS mobile satellite service (MSS) at Roi-Namur and Kwajalein, GPS VIZ at Lae and Woja, and GPS Vaisala on the *Ronald H. Brown*. In the appendix, we describe a comprehensive quality control procedure applied to all soundings. As part of this procedure, all soundings are interpolated onto a common set of pressure levels with 25-hPa spacing from 75 to 825 hPa, 10-hPa spacing from 850 to 1000 hPa, and a surface level.

In this paper, we will focus on synoptic-scale variability. We regard the sounding from each site as a separate sample of a similar time-varying large-scale environment (which is what we wish to characterize) with smaller-scale local fluctuations. To filter out the local fluctuations, we can average the soundings across all the sites reporting at a given time. However, different sites had different sounding frequencies. Furthermore,

there are small systematic differences between soundings at different sites likely related to both differences in instrumentation and mean spatial gradients, which we will document in section 3. These differences can alias into the time variability of a simple average of available soundings as the set of reporting sites changes.

To avoid this problem, we adopted the following averaging procedure. First, we calculated a perturbation sounding of each variable (temperature, relative humidity, and wind components) at each site and time by subtracting the site time-mean sounding of that variable. We then averaged all the perturbation soundings available at each reporting time to get an array-averaged perturbation sounding for that time. These perturbation soundings were constructed at 3-hourly resolution. By averaging the time-mean soundings for the five sites, we also obtained an array-averaged time-mean sounding. Adding this to the array-averaged perturbation sounding gave the time-varying array-averaged sounding. In this paper we will use this and the array-averaged perturbation soundings, binned to either daily (Figs. 8, 9, and 10) or 6-hourly (Fig. 11) resolution.

b. *GMS infrared*

We obtained infrared equivalent blackbody temperature (T_{BB}) observed by the Japanese Geostationary Meteorological Satellite (GMS) from the Space Science and Engineering Center at the University of Wisconsin. For analysis, we downgraded the data from its native pixels to a regular grid with $0.5^\circ \times 0.5^\circ$ and hourly resolution. Some gaps exist, most of no more than a few hours (see Fig. 4). These gaps were not filled.

A color animation of the GMS data is available as an electronic supplement to this study (available online at <http://dx.doi.org/10.1175/MWR2656supl1>). The animation was made at native pixel resolution and includes all available frames (gaps are skipped). Although viewing it is not necessary for interpreting any of the other results in this paper, we have found it illuminating to look at the spatiotemporal distribution of convection directly in this animation.

c. *Radar*

During KWAJEX, the permanent Kwajalein S-band Doppler radar (Schumacher and Houze 2000) made one 360° surveillance scan and two 360° volume scans every 12 min (YUT). Rain-rate maps were derived from the radar reflectivity data at the lowest elevation angle of the volume scans. Nonmeteorological echoes such as ground clutter from nearby islands, sea clutter, and second-trip echoes were removed. The polar data were interpolated on to a $2 \text{ km} \times 2 \text{ km}$ Cartesian grid using the National Center for Atmospheric Research (NCAR) SPRINT software. The mapping from reflectivity to surface rain rate takes into account the increasing altitude of the radar data with increasing range by application of mean

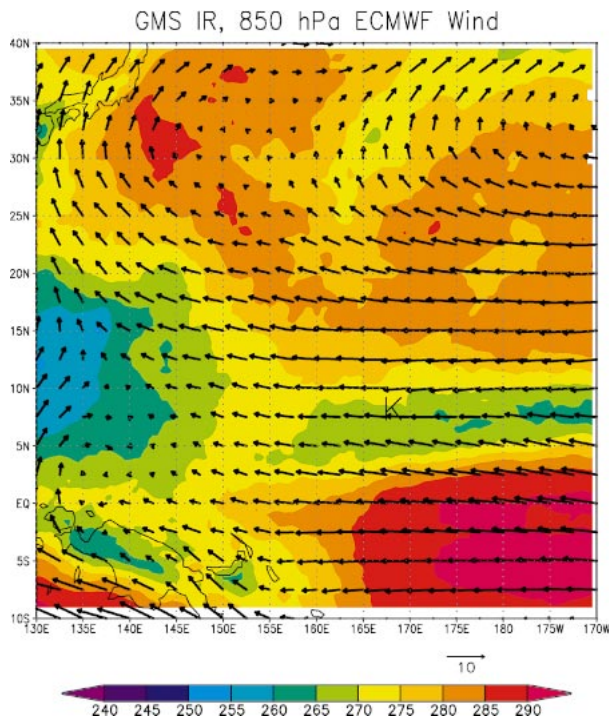


FIG. 2. Time-mean (21 Jul–15 Sep) 850-hPa vector wind (m s^{-1}) and GMS equivalent blackbody temperature (T_{BB} , K) for the KWAJEX period. Letter K indicates the location of Kwajalein.

profiles of relative Z variation in convective and stratiform precipitation. The Z – R relation employed was derived from Joss–Waldvogel disdrometer data obtained on Kwajalein. Further details on the rainmap processing can be found in Houze et al. (2003, manuscript submitted to *J. Hydrometeor.*). We utilize version 2 of the University of Washington calibration-corrected Kwajalein radar site maps (TRMM Product 2A53UW) available from the NASA Goddard Distributed Active Archive Center. In this paper, the rain maps were averaged areally over the entire area of good data, which is a circle of 150-km radius minus a 17-km-radius circle at the center (a total area of approximately $70\,000 \text{ km}^2$), and averaged in time to hourly or daily time scales.

d. *Other data*

We used total column water vapor path retrieved from microwave emissions at four frequencies from all available overpasses of the Special Sensor Microwave Imager (SSM/I) satellites, obtained from Remote Sensing Systems Inc. We binned these data to daily time resolution and averaged them onto a $2.5^\circ \times 2.5^\circ$ grid. For a number of meteorological fields, to provide spatial coverage beyond the sounding array, we used daily 0000 and 1200 UTC European Centre for Medium-Range Weather Forecasts (ECMWF) operational analyses, obtained from the Data Support Section of the National Center for Atmospheric Research. [Figure 3 uses NOAA

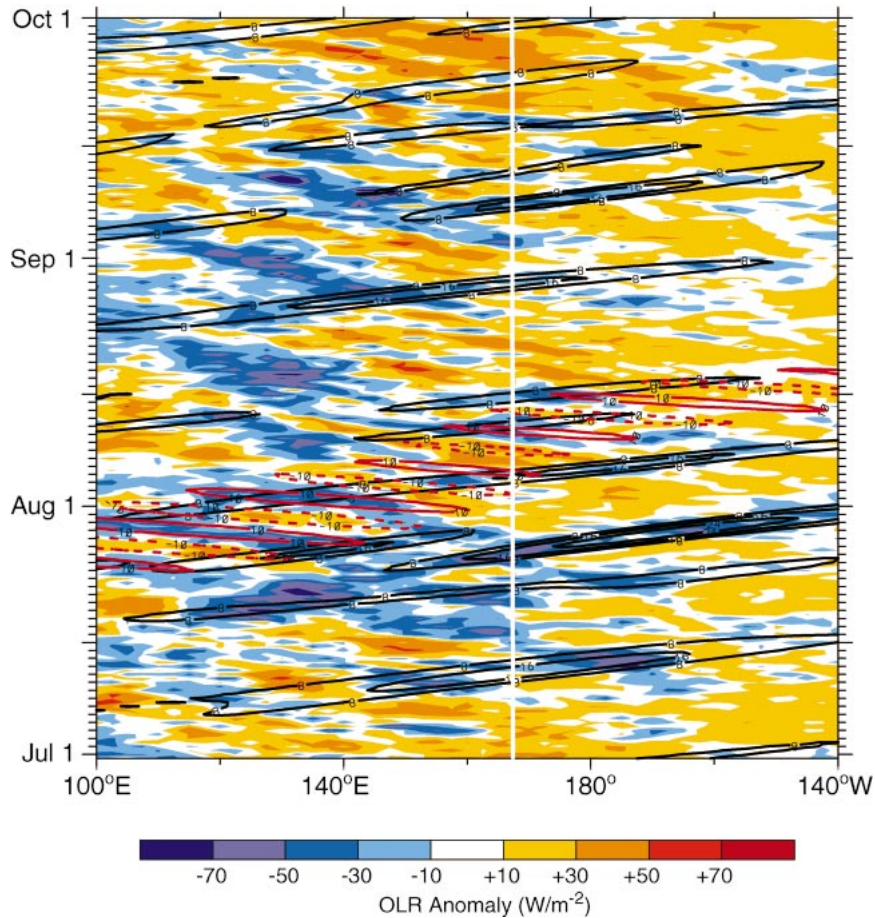


FIG. 3. NOAA OLR (W m^{-2}), averaged from 0° to 15°N , as a function of time and longitude, for the KWAJEX period. Color shading shows total OLR anomalies, black contours show anomalies identified with Kelvin waves as identified by spectral filtering, and red contours show anomalies associated with MRG waves. Vertical white line indicates longitude of Kwajalein.

outgoing longwave radiation (OLR).] Tropical cyclone tracks (used in the discussion in sections 3a and 3c) were obtained from a U.S. Naval Pacific Meteorological Center/Joint Typhoon Warning Center (USNPMOC/JTWC) report (McPherson and Stapler 2000).

3. Results

a. Large-scale overview

Kwajalein is located at the eastern edge of the western Pacific warm pool, in the vicinity of substantial gradients, longitudinal and latitudinal, in sea surface temperature (SST) and other variables related to it such as precipitation and atmospheric humidity. Northern summer is the rainy season at Kwajalein, at 9°N , and in that season the weather has been found by prior investigators to be dominated by westward-propagating synoptic-scale disturbances (e.g., Reed and Recker 1971), although Straub and Kiladis (2002) found that eastward-propagating Kelvin waves are also common. In the sum-

mer of 1999 La Niña conditions were prevalent. At the longitude of Kwajalein, SST anomalies are not strongly determined by ENSO as it is defined by typical indices, but during KWAJEX they were negative. Further climatological context is provided by YUT.

Figure 2 shows the GMS T_{BB} and ECMWF 850-hPa vector wind averaged over the entire KWAJEX period. In many respects the pattern is typical of this region and season. Convective activity, indicated by low T_{BB} , is greatest in an east–west band, or intertropical convergence zone (ITCZ), centered between 5° and 10°N over most of the domain. In the westernmost region shown, convection is particularly active and covers a broader range of latitudes, extending northward into the subtropics. This may be considered the eastern extension of the continental Asian monsoon. This extension is sometimes given its own name, the western North Pacific monsoon (e.g., Murakami and Matsumoto 1994; Wang et al. 2001). Atypically by comparison to climatology, a region of relatively high T_{BB} separates the

oceanic ITCZ and monsoon regions, around 150°–155°E. Additional local minima in T_{BB} are located over New Guinea and a semistationary extratropical frontal feature oriented SW–NE in the northeastern quadrant of the domain. The low-level flow is easterly in the eastern tropical part of the domain. Farther west, at the ITCZ latitudes, the flow decelerates and turns toward the northwest, merging with the southwesterlies of the monsoon trough to the east of the Philippines. This southerly flow eventually becomes more westerly on the northern flank of the west Pacific subtropical high. There is a separate region of strong southerly flow coincident with the quasi-stationary frontal feature farther east, with a region of very weak mean flow to its west.

Figure 3 shows a time–longitude (Hovmoeller) plot of OLR anomalies (shaded) and contours of space–time-filtered OLR for several Kelvin wave and mixed Rossby–gravity (MRG) wave events during the KWAJEX period, all averaged from 0°–15°N. The OLR anomaly fields were calculated by subtracting the first three harmonics of the seasonal cycle from the total field OLR for the period 1979–2001. The filtering was done using the procedure outlined in Wheeler and Kiladis (1999). General westward propagation of the OLR perturbation field in Fig. 3 is occasionally interrupted by the rapid eastward propagation of convective envelopes (negative OLR perturbations), which have a phase speed of around 15 m s⁻¹. This phase speed is characteristic of convectively coupled Kelvin waves (Takayabu and Murakami 1991; Wheeler and Kiladis 1999; Straub and Kiladis 2002, 2003), many of which originate well to the west of, and propagate through, the KWAJEX study region and into the eastern equatorial Pacific. A prominent example is seen there on 26 July. The predominant westward-moving convective regions actually have maximum amplitudes to the west of the longitude of Kwajalein, and these move at around 6 m s⁻¹, a speed typical of easterly waves over this region. At times, however, much faster westward propagation of closer to 20 m s⁻¹ is seen that projects well onto the MRG-filtered OLR field, and is typical of MRG waves over this domain (Liebmann and Hendon 1990; Takayabu and Nitta 1993; Dunkerton and Baldwin 1995; Wheeler et al. 2000). A packet of MRG disturbances disperses eastward from the westernmost Pacific starting in late July, and affects the Kwajalein region in early August, to be discussed further later. Based on the spectrally filtered OLR fields, the 30–60-day Madden–Julian oscillation was inactive during this period at the longitudes of the Marshall Islands and so was not a factor during KWAJEX.

A higher-resolution Hovmoeller plot of GMS T_{BB} is shown in Fig. 4 for a smaller longitudinal domain than that shown in Fig. 3. Figure 4 also shows the time series of areally averaged rain rate from the Kwajalein radar. The plot is dominated by a mix of slower and faster westward propagation as before, with eastward Kelvin wave events also evident, especially near the beginning and end of the record.

Figure 5 is a plot of ECMWF 850-hPa meridional wind, v , also averaged from 0° to 15°N. The 3–6-day variability seen in Fig. 3 is evident here as westward-propagating features of varying phase speed, which generally increase in amplitude to the west of Kwajalein. The strongest minima in T_{BB} , and strongest maxima and minima in v , tend to occur at the westernmost longitudes and to be associated with tropical cyclones: Tropical Storm Neil and Typhoon Olga in late July and very early August, Typhoon Sam between 16 and 21 August, Typhoon Wendy just before 1 September, and Tropical Storm Zia around 12 September. The approximate date at which these storms crossed 130°E and had reached at least tropical storm strength is marked in red on the left side of Figs. 4 and 5.¹ In all of these cases, the strong T_{BB} minima on the western edge of Fig. 4 correspond to the early phases of these storms' development, when they had begun to be tracked by USNPMOC/JTWC but had not reached their maximum intensities, which typically occur farther northward and/or westward than the range covered by the figure. At any given longitude, the maxima in v (southerlies) are more clearly related to the tropical cyclones than are the minima (northerlies), because they correspond to cyclone centers that have moved farther to the west, by which time they have usually intensified. For the same reason, the maximum southerlies tend to occur slightly after the typhoon IR minima.

In addition to westward-propagating disturbances and tropical cyclones, there are some features that defy simple interpretation. There are times, such as around 15 August and 170°E–180°, when one sees T_{BB} minima that are oriented horizontally over scales of 1000 km or more, indicating “blowups” of convection that occur apparently instantaneously, or at least too fast for any finite longitudinal propagation speed to be detected, over that length scale. These events often seem to be associated with weak Kelvin waves that only intermittently trigger significant convection. In the case of the 15 August blowup, there is some hint that interaction of weak Kelvin and MRG waves may have helped initiate the blowup, but the relation of convection to preexisting large-scale waves is far from deterministic.

Figure 6 shows a Hovmoeller plot of SSM/I water vapor path (WVP), in color, with ECMWF 850-hPa zon-

¹ These labels are somewhat subjective and imprecise. Some storms remained to the west of 130°E but came close, and others crossed 130°E before reaching tropical storm strength; the time at which the storm was subjectively judged to have the strongest influence on the plotted v was chosen based on a combination of proximity to 130°E and storm strength. Several other named or numbered storms occurred during the period but are not listed here because they either never reached tropical storm strength (tropical depressions 14W, 15W, and 18W) or because they either remained far west of 130°E (Typhoon York), or passed to the north rather than west of the averaging region of the figure and thus did not strongly influence v (Typhoons Tanya and Virgil).

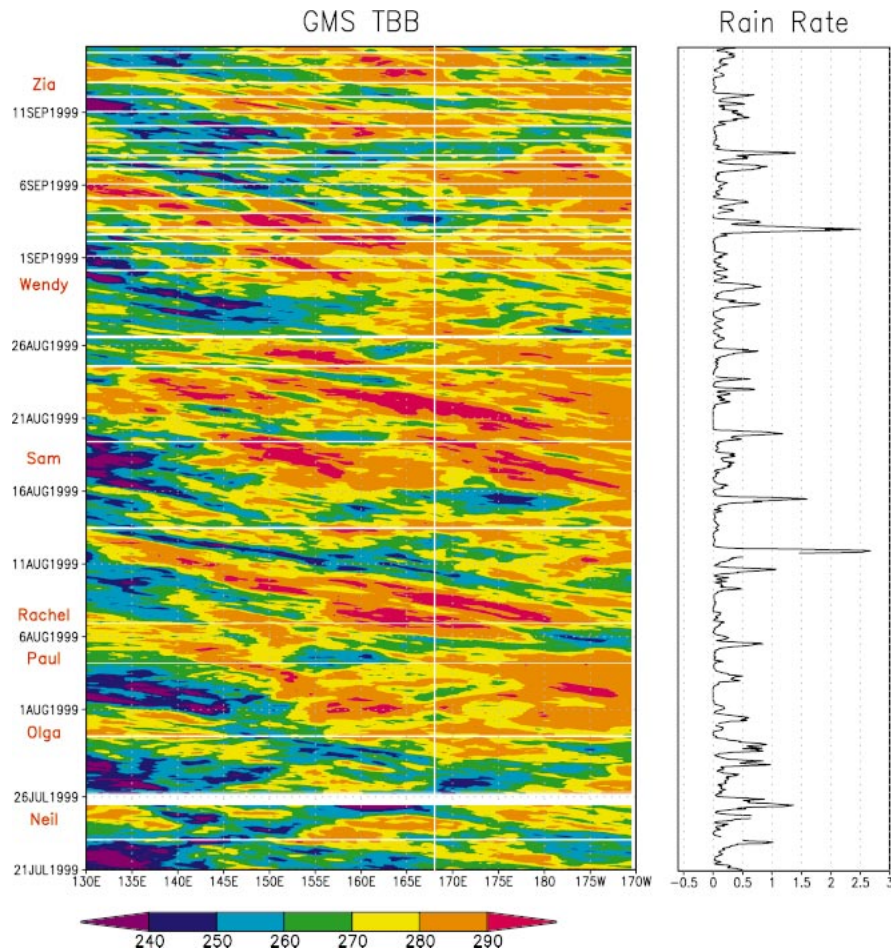


FIG. 4. (left) GMS T_{BB} (K) averaged from 0° – 15° N, as a function of time and longitude. (right) Time series of hourly and areally averaged rain rate (mm h^{-1}) from the Kwajalein radar. Vertical white line indicates longitude of Kwajalein, and words in red at left indicate tropical cyclones; see text for details.

al wind, u superimposed. Only a few contours are used for the u field for clarity. The WVP appears smoother than the other fields, in part because its time resolution is daily (as opposed to 12-hourly for the ECMWF data and hourly for the GMS data), but overall it is dominated by the same synoptic-scale westward phase propagation as in the previous two figures. To a greater extent than in those figures, the WVP shows slow eastward energy propagation along with the faster westward phase propagation in the first half or so of the period. This is expected for MRG waves in this region based on previous work using more sophisticated analysis techniques (Liebmann and Hendon 1990; Dunkerton and Baldwin 1995; Dickinson and Molinari 2002), but is visible here with no temporal filtering or other processing of any kind.

The u field shows less evidence of westward propagation, as is expected since the MRG waves and tropical depression (TD) type disturbances, which are typical of

this region, are known to be more manifest in v than u . Our inclusion of u with WVP in this figure makes two points. First, the longitude at which the zonal wind is zero roughly tracks in time with the maximum in WVP, and always remains well to the west of Kwajalein. Between 150° E and 180° , the time-mean WVP decreases 10 mm in a region of deep (but variable) mean easterlies. Hence, it is plausible that zonal moisture advection is playing a significant role in the variability of WVP around Kwajalein. To the extent that a moist troposphere is required to sustain deep convection, moisture advection may play an important role in modulating precipitation in this region on synoptic scales. This may help explain why the correlation between wind speed (surface latent heat flux) and precipitation observed in the east Pacific ITCZ by Raymond et al. (2003, hereafter RAY) is not observed at Kwajalein, as will be seen later (Fig. 10). In particular, stronger low-level easterlies have two counteracting effects on WVP, namely advective

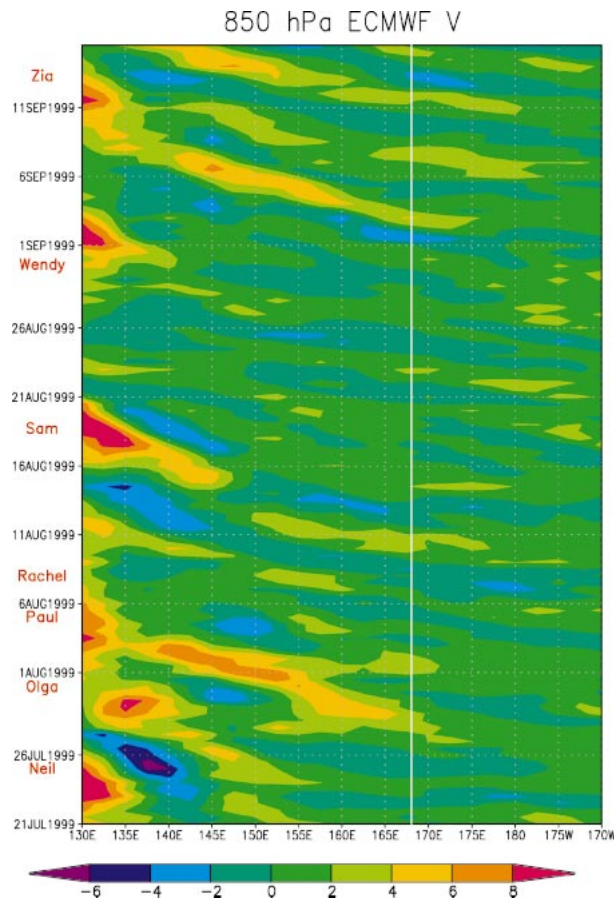


FIG. 5. The 850-hPa meridional wind (m s^{-1}) averaged from 0° to 15°N , as a function of time and longitude. Longitude of Kwajalein and times of tropical cyclone influence as in Fig. 4.

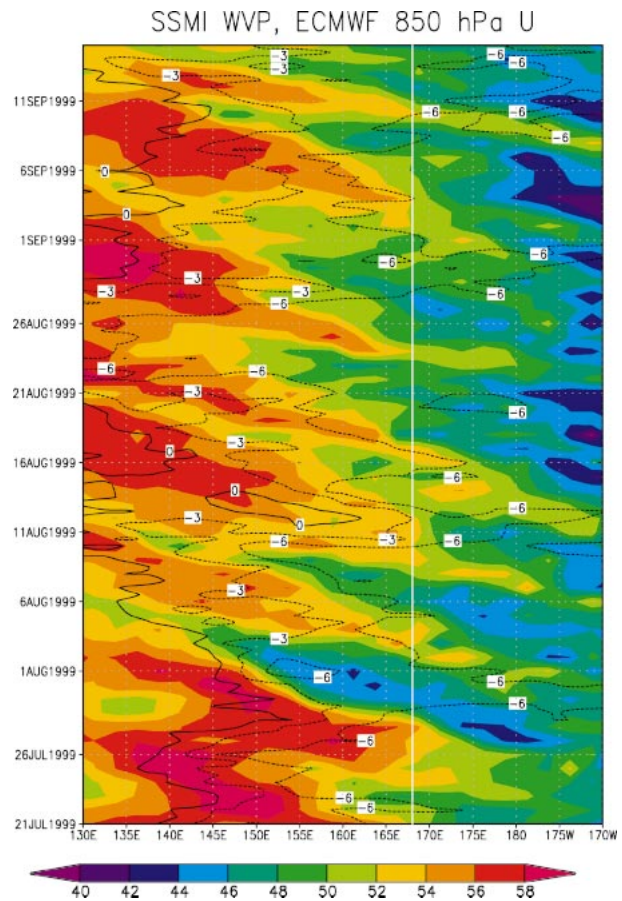


FIG. 6. The 850-hPa zonal wind (m s^{-1} , contours) and SSM/I column WVP (mm, color shading), both averaged from 0° to 15°N , as a function of time and longitude. White line indicates longitude of Kwajalein.

drying and surface flux-induced moistening. We intend to investigate this further in future work.

b. Soundings

1) TIME-MEAN AND TIME SERIES

Figure 7 shows time-mean soundings of moist static energy, saturation moist static energy, relative humidity, and the wind components at the five sites. Their differences reflect systematic geographical gradients in all quantities, perhaps sampling errors, and, probably, systematic measurement biases, particularly in the case of humidity. The mean thermodynamic sounding is very similar to other disturbed tropical regions and exhibits deep conditional instability. A hint of a mixed layer between the surface and 960 hPa can be seen as a low-gradient region in the moist static energy profiles. Easterly winds maximizing around 600 hPa characterize the lower and middle troposphere, switching to westerlies between 300 hPa and the tropopause. The meridional winds between the surface and 850 hPa have a stronger northerly component at Lae than at Woja (the south-

ernmost site, with the same type of sounding system as Lae), which may be indicative of low-level meridional convergence into the ITCZ. Similarly, in the upper troposphere, northerly flow at Woja gives way to near-zero and then southerly flow at more northern stations, consistent with mass outflow from the ITCZ at upper levels. It is possible that time-mean wind differences, for instance those between the *Ronald H. Brown* and Kwajalein, might be associated with the different wind sounding systems used at those locations (MSS at Kwajalein and GPS Viasala on the *Ronald H. Brown*), though we know of no specific evidence of biases in wind measurements (as opposed to humidity measurements) associated with particular sonde types. While the general shape of the relative humidity profiles is similar at all sites, the relative humidity (and hence the moist static energy) measured on the *Ronald H. Brown* was systematically 5%–10% lower than at other sites, perhaps due to the different (Vaisala Humicap) humidity sensor in use there than at the other sites.

In Fig. 8 we show time-height cross sections constructed from daily means of the array-averaged tem-

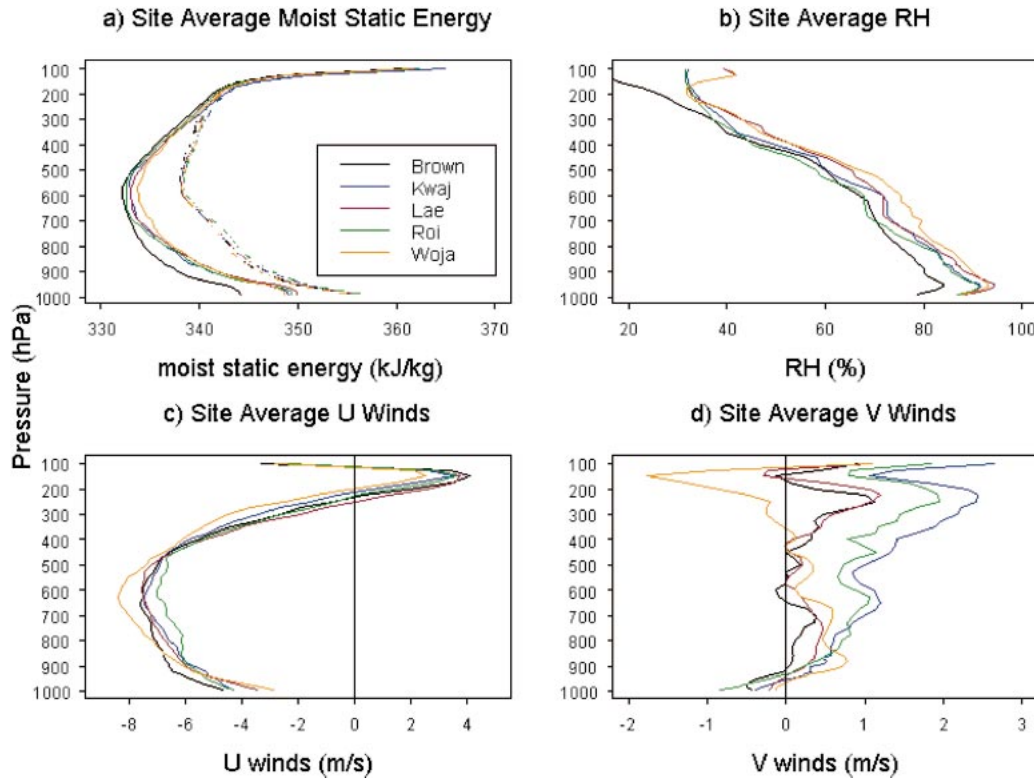


FIG. 7. The 25 Jul–14 Sep 1999 time-mean soundings at the five KWAJEX sites: (a) moist static energy (solid) and saturation moist static energy (dashed), (b) relative humidity, (c) zonal wind, and (d) meridional wind.

perature perturbation (T), relative humidity (RH), zonal velocity (u), and meridional velocity (v). A time series of daily mean rainfall is superimposed at the bottom of each plot, and vertical lines indicate three events that we will discuss in detail in section 3c. All fields show variability on synoptic (3–5 day) and longer time scales, with synoptic variability particularly evident in v and lower-frequency intraseasonal variability particularly evident in u . In particular, u seems to show synoptic to intraseasonal variability around 150–200 hPa that does not appear closely connected to the lower troposphere. The lower-tropospheric signals are the ones that we expect to be most closely related to the weather-producing synoptic-scale disturbances in this region (e.g., Wallace and Chang 1969; Reed and Recker 1971; Nitta and Takayabu 1985; Lau and Lau 1990; Holland 1995; Chang et al. 1996; Sobel and Bretherton 1999).

For westward-propagating disturbances, increasing time can be associated with increasing eastward distance, assuming a static disturbance structure that moves at a fixed speed. As we saw above, not all disturbances of interest propagate westward, but the bulk of the higher-frequency fluctuations seen in Fig. 8 do. In section 3c, we will examine some of the synoptic time scale fluctuations that dominate the v field more closely. Some are picked out by spectral filtering as MRG waves, while others appear to be “tropical depression type” (TD type) disturbances. The former term is defined by linear wave

theory and by spectral filtering (e.g., Wheeler and Kiladis 1999). We define the latter as any westward-propagating, synoptic-scale disturbance, with strong signals in lower-level v and vorticity, that is sufficiently off-equatorial that it cannot be classified as an MRG wave; also, TD-type disturbances generally propagate more slowly than MRG waves. The TD-type category can include vortices with closed streamlines and absolute vorticity contours (such as true tropical depressions) as well as short Rossby waves that are not equatorially trapped (e.g., Sobel and Horinouchi 2000); we view the difference as mainly a function of amplitude. Here we avoid entirely the term “easterly wave” as it is not clear to us whether its use in the western Pacific includes MRG waves, which we wish to distinguish here.

For the roughly 3–6-day fluctuations in Fig. 8, an eastward tilt with height is evident at times throughout most of the troposphere, especially in the v and T fields, with a westward tilt above around 300 hPa. This is consistent with the mean vertical structure of MRG waves (Wheeler et al. 2000). The observed vertical tilt of synoptic-scale westward-propagating disturbances in this region varies from eastward to westward with height (e.g., Reed and Recker 1971; Serra and Houze 2002; Petersen et al. 2003), being generally expected to depend on the vertical shear of the basic state (e.g., Holton 1971). There is virtually no evidence of westward tilt (below the uppermost troposphere) in Fig. 8. In fact, at

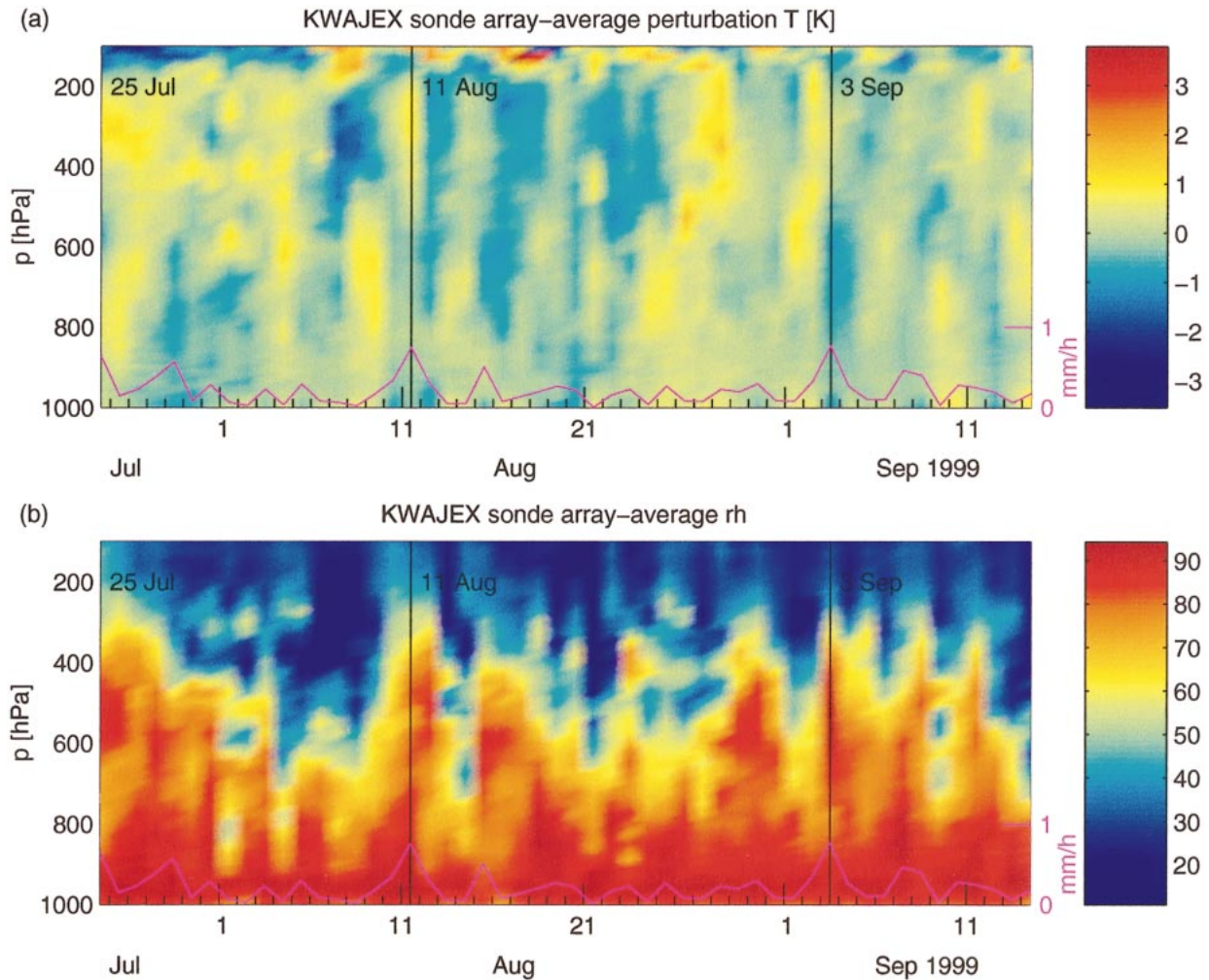


FIG. 8. Time–height plot of rawinsonde daily mean array averages during KWAJEX: (a) temperature perturbation, (b) relative humidity (with respect to liquid water), (c) u , and (d) v . Time series of daily mean rain rate (mm h^{-1}) is superimposed at the bottom of each plot, and vertical lines indicate 25 Jul, 11 Aug, and 3 Sep, the times of the three events discussed in detail in section 3.

the temporal resolution of this figure, changes appear to occur more often simultaneously throughout a large depth of the lower to midtroposphere.

Some general statements on the relationship between precipitation and the large-scale flow and thermodynamic fields during KWAJEX can be made by simple inspection of Fig. 8. Precipitation occurs preferentially during periods of low-level westerly flow, with deep easterly flow being dry. This relationship is typical of this region of the western Pacific on submonthly and lower-frequency intraseasonal time scales (Chen et al. 1996; Kiladis and Weickmann 1997; Lucas and Zipser 2000). A somewhat less robust relationship is seen between precipitation and enhanced southerly flow, especially toward the end of the record. This is typical of an off-equatorial ITCZ location, where precipitation tends to be associated with poleward flow in westward-propagating disturbances at this longitude (Reed and Recker 1971).

Throughout most of the troposphere, temperature variations are small, 1 K or less, as expected, and show little obvious coherence with precipitation. The variations in RH are large, especially in the 400–700-hPa layer, as is commonly observed in regions of deep convection (e.g., Reed and Recker 1971; Brown and Zhang 1997). There appears to be a strong relationship between moistening and precipitation, as will be verified in the next section.

2) INSTANTANEOUS AND LAGGED RELATIONSHIPS BETWEEN THERMODYNAMIC VARIABLES

In this section we show scatterplots of various daily averaged thermodynamic quantities versus one another. Sounding-derived quantities are computed from the daily mean array-averaged soundings, which are an average of typically 15–30 individual soundings scattered around the five sounding sites. The random sampling

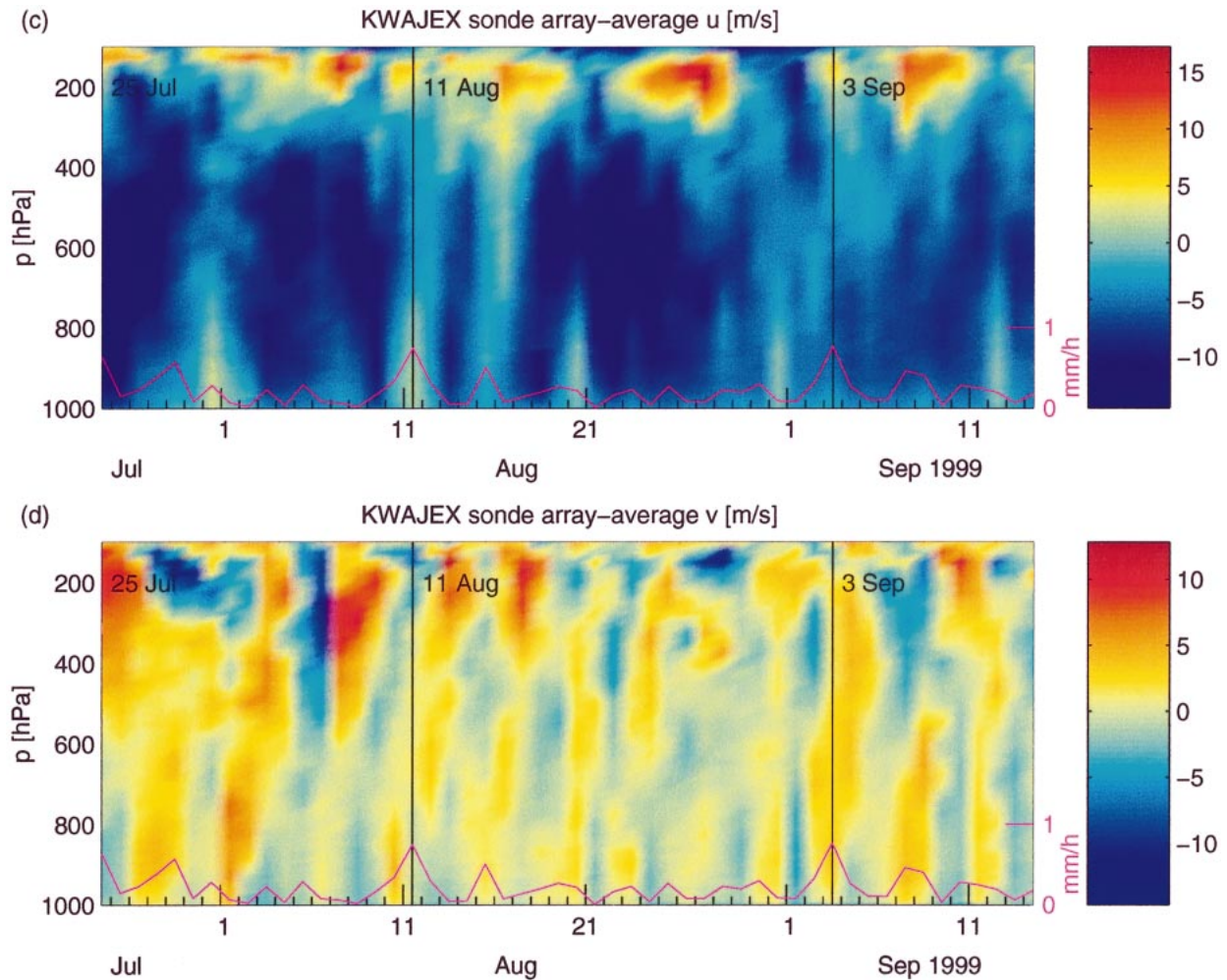


FIG. 8. (Continued)

uncertainties of the daily mean array-averaged soundings, estimated in the appendix, are much smaller than the typical magnitudes of the perturbations in all variables shown here. All available rain maps (approximately every 12 min) are included in the daily averaged radar statistics. Hence, both the soundings and radar data provide meaningful daily averages over the space–time variability within 150 km of Kwajalein over the course of the day.

Relationships revealed in these plots can shed light on the degree and type of thermodynamic control of convection in this region on daily time scales. Several different hypotheses for such thermodynamic control have been proposed, though there is a broad similarity between them. Each assumes that in an appropriate ensemble average, convection acts to strongly regulate some measure of instability, which can be computed from the vertical profiles of temperature and moisture at a given location, keeping that measure at or near zero, or perhaps a nonzero but fixed value. Betts and Miller (1986) proposed a relaxed quasi-equilibrium closure in

which the measure of instability is relaxed smoothly toward zero by convection, rather than being held precisely at that value.

Arakawa and Schubert (1974) assumed that convection regulates the cloud work function, a measure of instability that includes entrainment (but not, in its original form, downdrafts) and is specific to a particular cloud type though it can be averaged over all cloud types to obtain a single value. Emanuel et al. (1994) assumed that in “strict quasi-equilibrium” (SQE) convection regulates convective available potential energy (CAPE) in such a way that perturbations in free-tropospheric temperature and boundary layer moist static energy track each other, keeping the whole sounding moist adiabatic. Downdrafts can be considered implicitly incorporated in this theory as they allow the free troposphere to influence the boundary layer, as well as vice versa. The simplest implementation of SQE assumes constant relative humidity in the free troposphere, so that moisture variability above the boundary layer does not enter the picture.

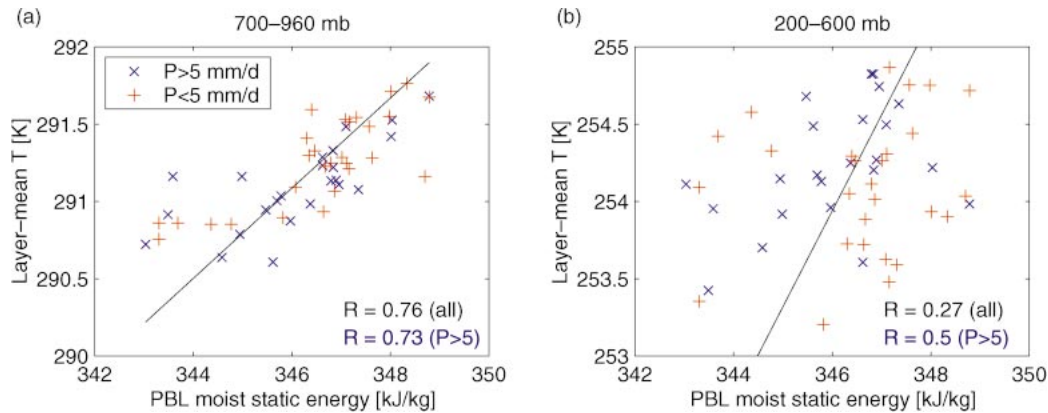


FIG. 9. Boundary layer moist static energy, h_b , vs layer-mean temperature for (a) the 600–960-hPa layer and the (b) 200–600-hPa layer, computed from the daily mean soundings. Blue indicates days with Kwajalein radar area-mean rain rate greater than 5 mm day⁻¹. Solid lines show regression slopes computed using all points, and correlation coefficients are shown at lower right, in blue for the precipitation-windowed points, in black for all points.

Raymond (1995) and Emanuel (1995) proposed “boundary layer quasi-equilibrium,” which is similar to SQE except that it requires only that the boundary layer stays in a dynamic equilibrium with the layer just above it and with the surface; the free troposphere is unrestricted. In this view lower-tropospheric moisture may be an important regulator of convection, as it influences the boundary layer through downdrafts and turbulent entrainment. Raymond (2000) proposed a still stronger role for free-tropospheric relative humidity, postulating that the precipitation rate is proportional to the inverse of the mass-weighted average of the saturation deficit over the troposphere. His argument was posed as a generalization of that of Neelin and Held (1987), who used the moist static energy budget to argue that lower-tropospheric moisture modulates the divergent tropospheric circulation by modulating the gross moist stability, which relates the rate of moist static energy export from a column to the mass circulation through it. This budget argument does not explicitly invoke downdrafts or any other specific aspect of convective physics. Whatever the specific mechanism, besides having been suggested theoretically, an important role for relative humidity in the lower free troposphere in controlling convection has been seen in some numerical modeling (e.g., Tompkins 2001; Sobel and Bretherton 2003) and observational studies (e.g., Sherwood 1999; Kingsmill and Houze 1999).

Figure 9 shows boundary layer moist static energy h_b , defined as the moist static energy averaged from 1000 to 960 hPa, versus layer-mean temperature for the layers 700–960 and 200–600 hPa. Points with an areal average Kwajalein rain rate greater than and less than 5 mm day⁻¹ are shown separately. SQE predicts that these plots should show a clear linear relationship with a positive slope. Previous tests of this theory on larger space and time scales using tropospheric-mean temperature have revealed that it is correlated with h_b , but with a smaller slope than predicted by SQE (Brown and

Bretherton 1997). Here, if all points are used, we see almost no relationship between h_b and the upper-tropospheric temperature, but a very close relationship between h_b and the lower-tropospheric temperature. The regression of the lower-tropospheric temperature variations on the boundary layer moist static energy is close to that predicted by a moist adiabat (the solid lines in Fig. 9), but slightly shallower. We speculate that this coupling, indicative of boundary layer quasi-equilibrium, is due to widespread, persistent shallow cumulus and congestus activity. Deep convection during KWAJEX was much more sporadic in space and time and, hence, was unable to produce the tight moist-adiabatic adjustment of upper-tropospheric temperature and boundary layer properties to one another as required for SQE. Consistent with this interpretation, if only days with strong rainfall (> 5 mm day⁻¹) are used, the correlation between h_b and upper-tropospheric temperature becomes significantly stronger (0.5 as opposed to 0.27). However, even in this case the regression slope is about a factor of 2 smaller than predicted by SQE, as found previously by Brown and Bretherton (1997).

Figure 10 shows scatterplots of layer-mean RH over the 700–960- and 200–600-hPa layers, CAPE (computed assuming conservation of pseudoadiabatic equivalent potential temperature for a surface parcel), and 1000-hPa wind speed, all versus areal-averaged rain rate. There is a positive correlation between rainfall and RH in both layers, though there is also much scatter. There are no points in the lower-right quadrants of the plots, indicating that rainfall cannot coexist with a dry troposphere. This is broadly consistent with the notion that rainfall is controlled or at least modulated by the saturation deficit over a layer deeper than the boundary layer. Nonetheless, we must be cautious in the interpretation of these correlations. There is little reason to think that the RH of the upper troposphere (200–600 hPa) can be strongly controlling convection. Presumably, the relationship between rainfall and RH in this

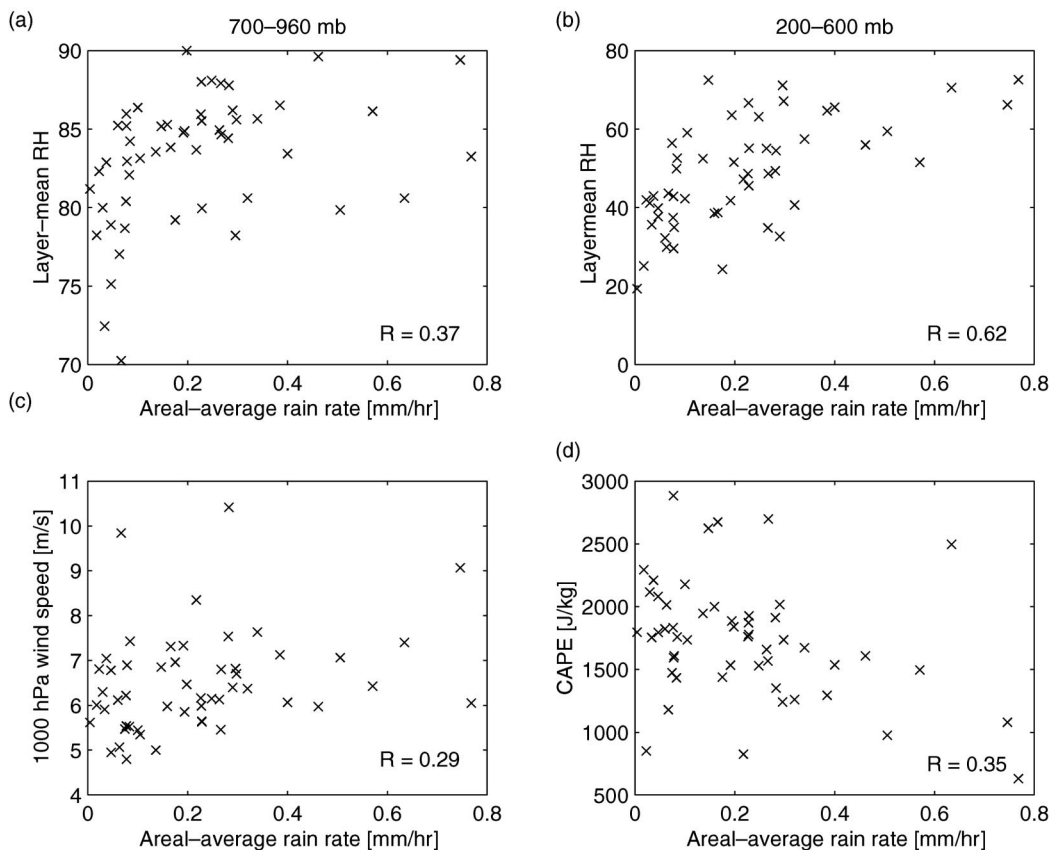


FIG. 10. Kwajalein radar area-mean rain rate (mm h^{-1}) vs (a) lower-level layer-mean RH, (b) upper-level layer-mean RH, (c) 1000-hPa wind speed (m s^{-1}), and (d) pseudoadiabatic CAPE (J kg^{-1}).

layer indicates the fact that only deep convection can bring moisture to this layer, so the convection controls RH here rather than the other way around. While we expect lower-tropospheric humidity to have a greater influence on convection than upper-tropospheric humidity on physical grounds, we cannot be entirely positive of the direction of causality for the lower troposphere either, on the basis of these instantaneous correlations alone. Lag correlations, on the other hand, can give stronger indications regarding the direction of causality, and these are shown below.

The relationship with CAPE is weak but slightly negative. This has been observed before (e.g., Thompson et al. 1979; Mapes and Houze 1992; Lucas and Zipser 2000) and is in contradiction to relaxation-type quasi-equilibrium closures (e.g., Betts and Miller 1986) to the extent that they are applied on daily time scales and that the measures of instability they attempt to remove are similar to pseudoadiabatic CAPE based on a non-entraining surface parcel. Broadly, the Betts–Miller scheme assumes that $Q \sim \text{CAPE}/\tau$, with Q representing vertically integrated convective heating and τ a time scale. Since τ is defined as positive, this predicts that precipitation and CAPE should be positively correlated.

The relationship with near-surface wind speed is

weak. If we remove the two outliers with largest surface wind speed, there is a slight positive relationship, which would be consistent with (though not proof of) some degree of control of convection by surface fluxes, to the extent that we take the surface fluxes to be largely controlled by the wind speed. From measurements in the eastern Pacific intertropical convergence zone, RAY find a much stronger relationship between a measure of convection [in their case, T_{BB} from the Geostationary Operational Environmental Satellites (GOES)] and surface wind speed than we do here. As suggested in section 3a (Fig. 6 and accompanying discussion), this may be due to the influence of zonal advection of the mean humidity gradient.

Figure 11 shows results of a lag-correlation analysis of lower-tropospheric RH, upper-tropospheric RH, and CAPE versus rain rate. For this calculation, all data were binned into 6-h intervals. The same calculation using daily data (not shown) hints at the results, but as can be seen from Fig. 11 the primary temporal structure occurs on a subdaily time scale. The black dotted lines at correlations of 0.2 are approximate two-sided 95% significance lines computed assuming 100 degrees of freedom (there are actually 216 sounding intervals, but

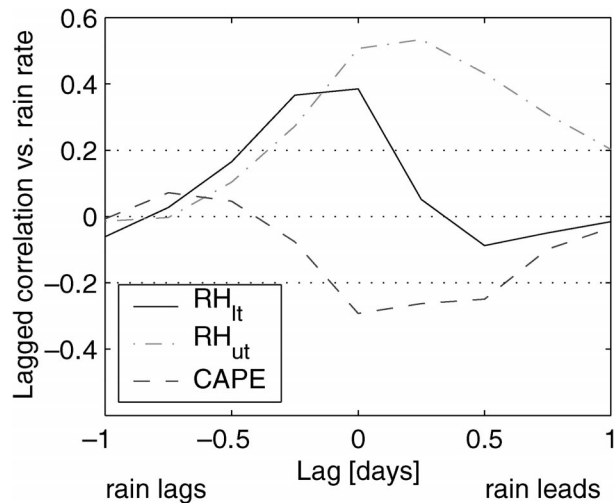


FIG. 11. Lag-correlation coefficients of lower-level layer-mean RH, upper-level layer-mean RH, and CAPE vs Kwajalein radar area-mean rain rate, computed at 6-hourly resolution. Dotted lines indicate significance at 95% confidence.

some are missing data and there is some serial correlation).

Lower-tropospheric RH is high prior to and during the time of maximum rainfall, then quickly drops to a negative correlation by 12 h following the rain event. The maximum correlation in upper-tropospheric RH lags rainfall by 6 h, as was found in previous studies (Sherwood and Wahrlich 1999; Straub and Kiladis 2002, 2003). This reinforces our preconceived notions that higher lower-tropospheric RH facilitates ensuing deep convection while upper-tropospheric RH is more an effect than a cause of deep convection. CAPE peaks prior to the onset of convection, and decreases to a minimum during and just after the heaviest rainfall, again in agreement with the composite results of Sherwood and Wahrlich (1999) and Straub and Kiladis (2003). We interpret the peak in CAPE prior to convection as indicating that instability in the sounding favors subsequent convection. The minimum in CAPE during and after the peak rainfall presumably results from the squelching of CAPE by convective or mesoscale downdrafts.

c. Synoptic view of specific events

In this section we focus on the spatiotemporal evolution and synoptic structure of the three largest rainfall events during the experiment, those of 25 July, 11 August, and 3 September. For each event, we present a magnified Hovmoeller plot of T_{BB} and WVP covering a 6-day period centered near the time of maximum rainfall at Kwajalein as measured by the ground radar. The T_{BB} gives a broad indication of the longitudinal propagation of the large-scale envelope of deep convection, while the WVP has some features, particularly in the 11 August case, that suggest possible mechanisms for

control of convection. For the 25 July and 3 September cases, we provide one latitude–longitude map of 850-hPa wind and relative vorticity, as well as T_{BB} , near the time of maximum rainfall at Kwajalein, to give a cursory descriptive sense of the synoptic situation for these events and to aid in the interpretation of the Hovmoeller plots. For the 11 August case we provide a sequence of six such maps covering a 6-day period.

1) 11 AUGUST

Fig. 12 shows a Hovmoeller plot of 0° – 15° N average T_{BB} and WVP for 8–14 August. The time series of radar rain rate is shown to the right of the Hovmoeller plot. The maximum areal-averaged rain rate for the 150-km-radius region centered around Kwajalein occurred at 2300 UTC on 11 August. The T_{BB} field is dominated by the westward phase propagation of first a minimum (which is only partially in the plot domain, in the lower-left corner), then a maximum indicating dry conditions, and then another minimum, the last part of which was associated with the main rain event at Kwajalein. This westward disturbance is moving at close to 15 m s^{-1} , somewhat slower than the typical MRG phase speed, although the impression from Figs. 3 and 4 is that it results from the eastward dispersion of energy associated with an MRG-like wave packet, dispersion that can also be seen in the alternating v component at 850 hPa in Fig. 5. The first passage of this T_{BB} minimum through the longitude of Kwajalein was actually not associated with much rainfall there; the rain at that time and longitude was mainly well south of Kwajalein.

Embedded within the general large-scale propagating waves, centered on about 0000 UTC on 11 August, there are four distinctly smaller-scale features with apparent eastward group propagation. This is much more rapid than the MRG group propagation seen over much longer time scales in Fig. 4. Tracing the packet along a SW–NE line, the main rain event at Kwajalein occurs somewhere between the third and fourth segments. It appears that either a westward-propagating wave crosses paths with a preexisting eastward-propagating one, or convection associated with a westward-propagating disturbance triggers an eastward-propagating wave. In either case the rain at Kwajalein appears to be most directly induced by the eastward-propagating wave, which according to the spectral filtering shown in Fig. 3 is a Kelvin wave although its amplitude is weak after the filtering. If this wave was preexisting, its role in modulating convection was secondary to that of the MRG wave prior to its interaction with the latter, since at times significantly earlier than 11 August the eastward-propagating T_{BB} signal is at best subtle, while the westward propagation associated with the MRG wave is easily seen.

On 8 and 9 August, before the disturbance begins to develop, we see an increase in WVP at the longitude of Kwajalein, possibly advected in by the lower-tro-

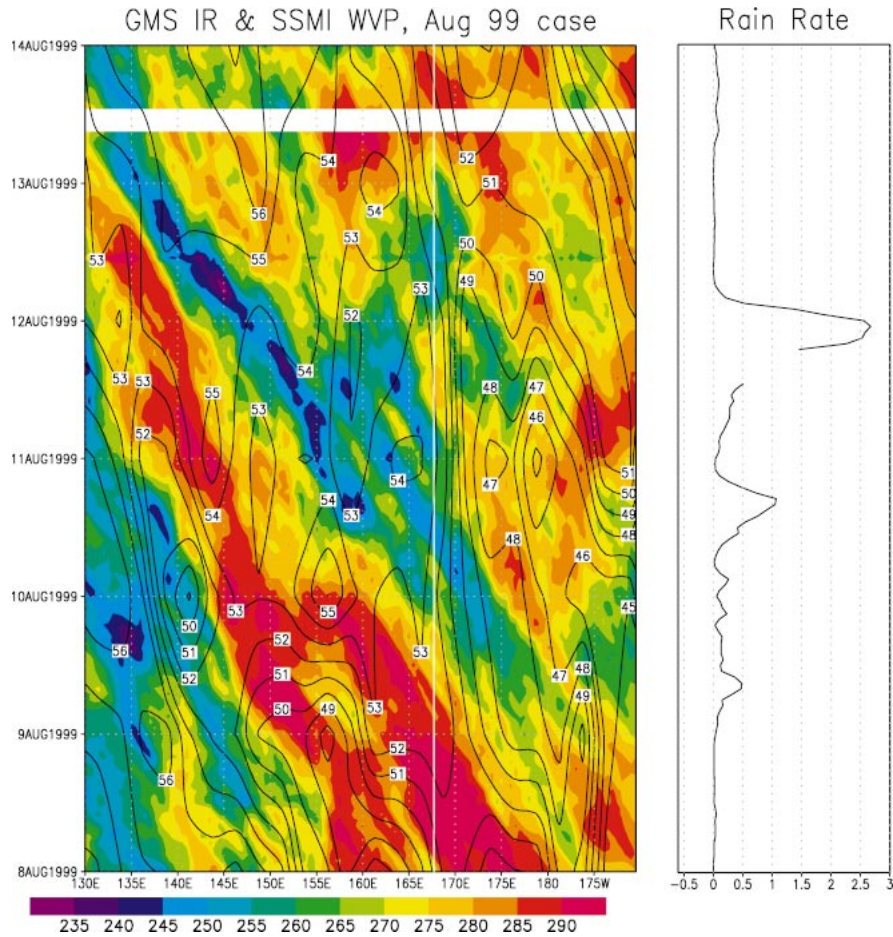


FIG. 12. (left) GMS T_{BB} (colors, K) and SSM/I WVP (contours, mm), both averaged from 0° to 15°N , as a function of time and longitude, from 8 to 14 Aug 1999. (right) Areal averaged Kwajalein radar rain rate (mm h^{-1}) for the same period. White line indicates longitude of Kwajalein.

pospheric easterlies. However, along the entire track of the MRG wave, it takes another day before substantial deep convection, indicated by lower $0^\circ\text{--}15^\circ\text{N}$ average T_{BB} , sets in. The points in the upper-left corner of Fig. 10 show that a moist column commonly exists for at least a day without extensive precipitation occurring; the relation between lower-tropospheric RH and rainfall is loose on daily time scales. The fact that moistening precedes rainfall in this case suggests that moistening might have been a causal influence on the development of the convection, a speculation that is somewhat reinforced by the statistical results in Fig. 11, which suggest the same thing in general.

Figure 13 shows a sequence of six synoptic maps, one per day at 1200 UTC, for the period 8–13 August. Each plot shows ECMWF horizontal vector wind and relative vorticity at 850 hPa, superimposed on GMS T_{BB} . In these maps we see the coherent westward propagation of a large-scale envelope containing convective disturbances, within a latitude band roughly from 0° to 10°N . The convection is just beginning to develop around the date line on 8 August and has reached the longitude of

Kwajalein by 10 August although the strongest rainfall did not occur at Kwajalein itself until 11 August. Between 10 and 11 August, the region of deep convection begins to broaden and fragment longitudinally, with some component starting to move eastward at the same time as much of it continues to move westward; this is the “forking” seen in Fig. 12. It is this eastward-moving component that was directly associated with the rainfall at Kwajalein. The spectral filtering shows a Kelvin wave signal associated with this component, but it is weak; gust front or gravity wave dynamics triggered by the storms to the west, or perhaps just the effectively stochastic “bubbling” of convection, may be equally plausible explanations for the precise timing of the peak rainfall at Kwajalein. Two other major features in these plots are the vorticity maximum near the NW corner of the plots for 8 and 9 August (partly visible on 10 August) associated with tropical depression 14W, and the extratropical cyclone that develops on 8 and 9 August around 30°N near the longitude of Kwajalein, and which has a strong frontal structure to its south by 11 August that gets stronger on 12 and 13 August.

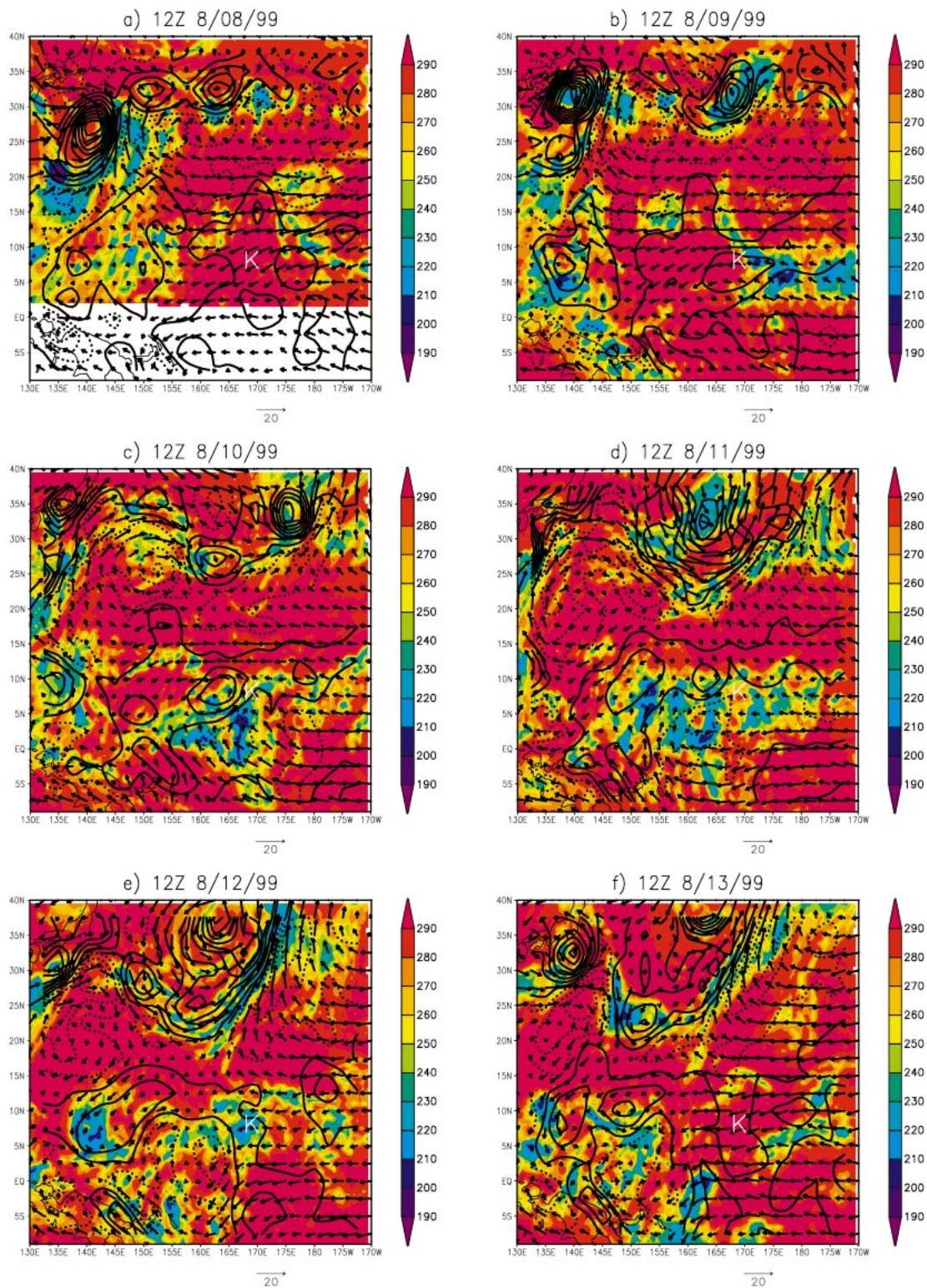


FIG. 13. (a)–(f) Sequence of synoptic maps for 11 Aug event. Each plot shows GMS T_{BB} (colors, K), 850-hPa vector wind (arrows, m s^{-1}), and 850-hPa relative vorticity (contours, 10^{-5} s^{-1} ; negative dashed). Letter K indicates location of Kwajalein. ECMWF data are from 1200 UTC analyses. GMS data are taken from the nearest available frame to 1200 UTC, if 1200 UTC data were not available; in no case is the difference more than a few hours.

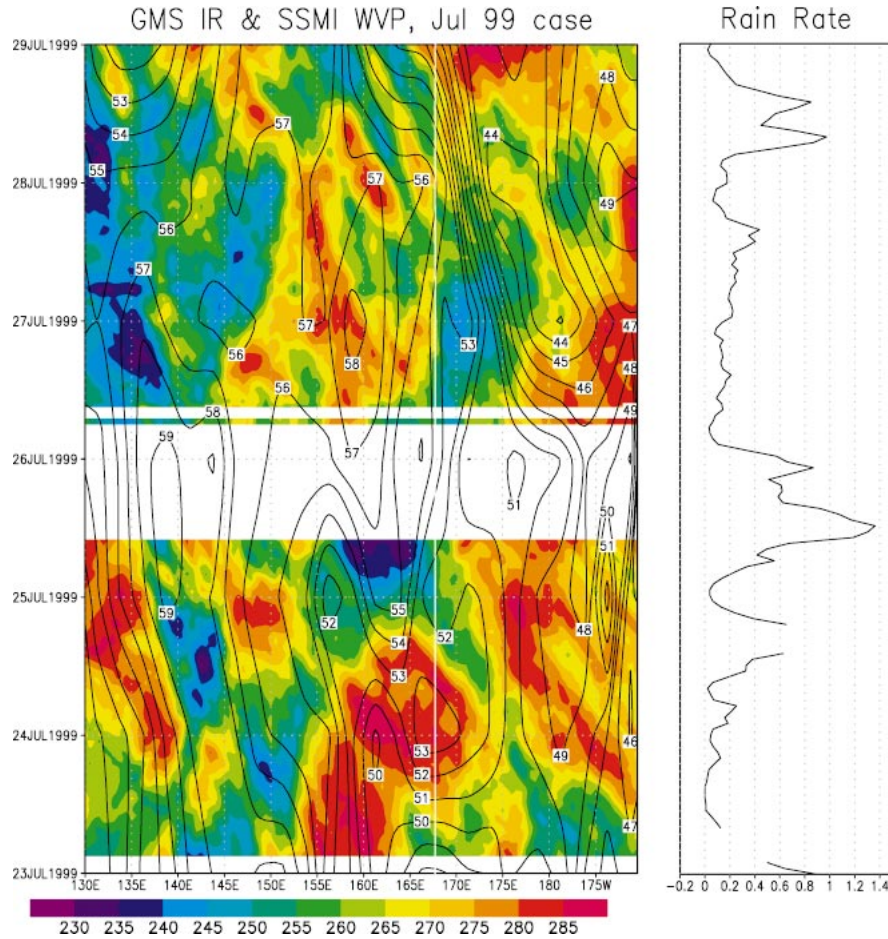


FIG. 14. (left) GMS T_{BB} (colors; K) and SSM/I WVP (contours, mm), both averaged from 0° to 15° N, as a function of time and longitude, from 23 to 28 Jul 1999. (right) Areal averaged Kwajalein radar rain rate (mm h^{-1}) for the same period. White line indicates longitude of Kwajalein.

Particularly on 11–13 August, some aspects of MRG structure are evident and corroborate the evidence from the spectral filtering. There is a synoptic-scale region of negative relative vorticity on the equator with strong southerly cross-equatorial flow on its western flank. Particularly on 11 August there is some tendency for the convection to be centered where we would expect to have convergence according to dry linear theory for an MRG wave, in the poleward flow to the northwest of the negative vorticity anomaly, although this relationship is far from tight and at other times the convection is much more broadly distributed.

Some features evident in this event are typical of this region and season, but cannot be associated with an MRG structure per se. From 10 through 13 August we can clearly see a wave train in the vorticity field, connecting the negative vorticity anomaly discussed above to TD 14W over two distinct wavelengths. The off-equatorial vorticity anomalies have no counterpart in linear equatorial MRG solutions. This overall structure is, however, common over the tropical western North Pacific. Dickinson and Molinari (2002) show a similar

case using winds filtered in the time domain to 6–10-day frequencies; here no filtering is needed to see either the MRG disturbance or the SE–NW-aligned wave train, which coexist here although they are often studied independently. Dickinson and Molinari argue that vorticity anomalies associated with MRG waves can serve as seed disturbances for tropical cyclogenesis. In this case, this does not occur. There may well be an influence in the other direction. We strongly suspect that TD 14W is to some degree driving this wave train through Rossby wave radiation (Davidson and Hendon 1989; Holland 1995; Sobel and Bretherton 1999) both because straightforward vorticity dynamics indicates that a forced vortex on a β plane should produce such a response (e.g., Flierl et al. 1983; McWilliams et al. 1986) and because the TD precedes the formation of the wave train in time.

2) 25 JULY

Figure 14 shows a Hovmöller plot of 0° – 15° N averaged T_{BB} IR and WVP, together with the rain-rate time series, this time for 23–28 July. The maximum areal

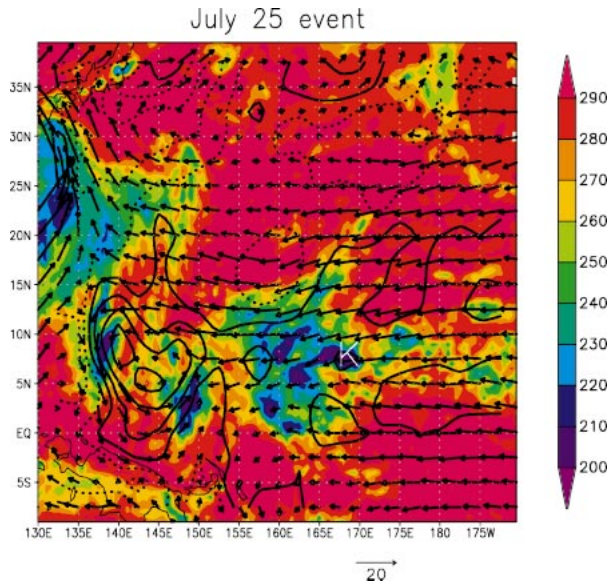


FIG. 15. Synoptic map of GMS IR (1000 UTC) and ECMWF 850-hPa wind and vorticity (1200 UTC) for 25 Jul event; all fields plotted as in Fig. 13.

precipitation rate around Kwajalein occurred around 1200 UTC on July 25, unfortunately during a substantial gap in the GMS data. Nonetheless, a fairly good idea of the spatiotemporal evolution of this event is obtainable from the available data. Eastward propagation of the IR minimum is clearly evident. Figure 3 shows that this convective envelope originated at around 110°E in mid-July, and propagated eastward at the typical Kelvin wave phase speed of 15 m s^{-1} through the KWAJEX region and then into the eastern Pacific by the end of the month.

Some broad characteristics of the WVP can be summarized. Although there is a weak east–west moisture gradient during this period, there are no very dry regions ($\text{WVP} < 50 \text{ mm}$) anywhere westward of 170°E. Deep convective systems occur on and off throughout the ITCZ region, extending east almost to the date line, in the several days preceding the period shown. The Kelvin wave evident in T_{BB} shows good correlation with the WVP, and WVP decreases rapidly with the passage of the wave.

Figure 15 shows the GMS IR at 1000 UTC on 25 July (the closest time to the maximum rainfall, at around 1400 UTC, for which the GMS data were available) superimposed on ECMWF 850-hPa wind and relative vorticity at 1200 UTC. The large convective system centered around 160°–165°E with a horizontal scale on the order of 1500 km was responsible for the rain event at Kwajalein. This system has no clear vorticity signal, but a strong zonal wind speed convergence signal, as expected for a Kelvin wave. The low-level zonal wind in Fig. 3 also shows this signal well, with easterlies giving way to westerly flow after the passage of the

wave, similar to that seen in the case in the eastern Pacific studied by Straub and Kiladis (2002).

Some other interesting synoptic activity is also evident in Fig. 15. The IR minimum and strong southerlies around 25°N along the western boundary of the plot domain are associated with the tropical depression that would, within 12 h, be upgraded to Tropical Storm Neil. A second vorticity maximum, centered roughly around 5°N, 145°E, has some convection associated with it. Inspection of maps from the preceding several days (not shown) suggests that the latter vorticity maximum results at least in part from downstream energy propagation, or (equivalently) Rossby wave radiation from the tropical cyclone, as described in a number of previous studies (e.g., Holland 1995; Sobel and Bretherton 1999), and which typically results in wave trains with a SE–NW tilt, as here, and as in the 11 August event described above.

3) 3 SEPTEMBER

Figure 16 is a Hovmoeller plot identical in format to Figs. 14 and 12, but for the period 1–7 September. The maximum area-averaged rain rate occurred at 0100 UTC on 3 September. Westward phase propagation similar to the 11 August case is evident. A noteworthy difference between this case and both the 25 July and 11 August cases is that in this case the convection near Kwajalein appears to be the origin of the moving disturbance in the IR field, whereas in the other cases a preexisting moving disturbance was present prior to its arrival at Kwajalein. However, a preexisting maximum in WVP does appear to be being advected into Kwajalein from the east at the time of the Kwajalein convection. The spectral filtering, as noted earlier, does not pick up either a Kelvin or an MRG signal.

Figure 17, analogous to Fig. 15, shows GMS T_{BB} as well as 850-hPa wind and relative vorticity near the time of maximum rainfall on 3 September. From this plot, the lack of an MRG spectral signal is understandable. There is a vorticity maximum loosely associated with the convection near Kwajalein—roughly a quarter “wavelength” west of it in this particular plot—but only a small, weak vorticity minimum to its east, and that is centered off the equator at about 5°N and is associated with only weak cross-equatorial flow. So while in many ways the situation resembles that on 11 August, the whole disturbance is more off equatorial, and this results in much less MRG-type structure. The disturbance appears better classified as a TD type, which leads us to associate the westward phase propagation more with simple vorticity advection by the mean flow than with wave dynamics (Holland 1995; Sobel and Bretherton 1999). There is another convective region to the northwest around 20°N, 150°E, consistent with the SE–NW tilt typical of wave trains in this region and season (e.g., Lau and Lau 1990; Chang et al. 1996), and as seen in the previous two cases. However, the vorticity pattern

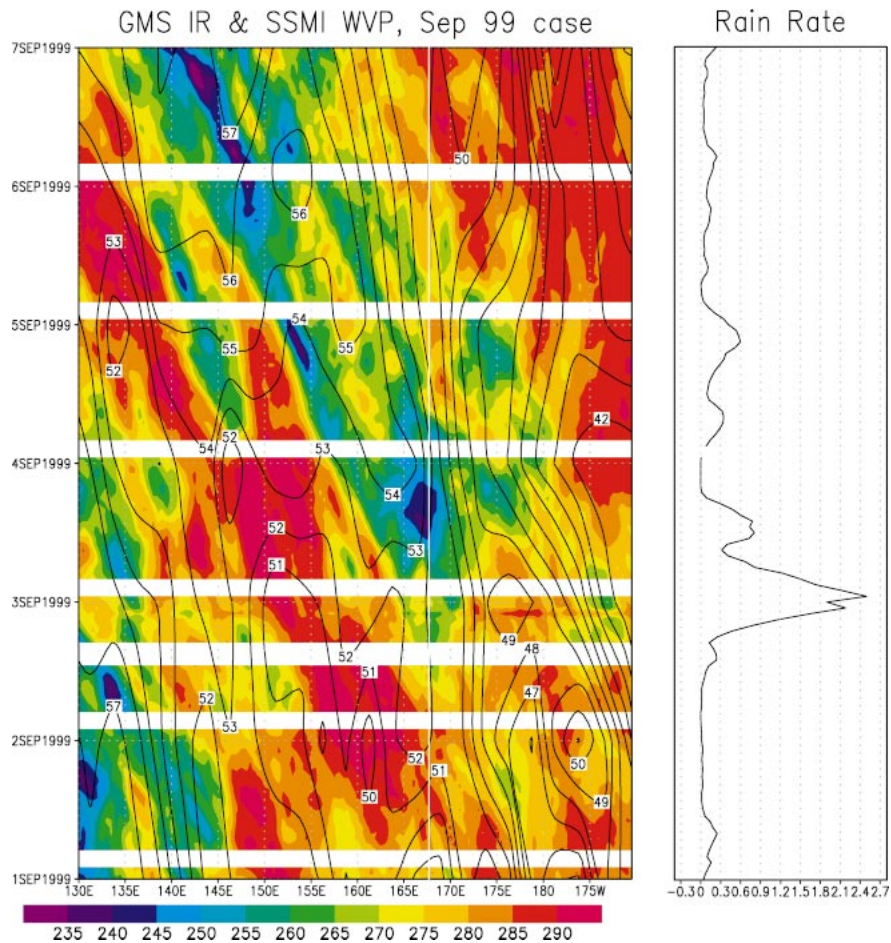


FIG. 16. (left) GMS T_{BB} (colors, K) and SSM/I WVP (contours, mm), both averaged from 0° to 15°N , as a function of time and longitude, from 1 to 6 Sep 1999. (right) Areal averaged Kwajalein radar rain rate (mm h^{-1}) for the same period. White line indicates longitude of Kwajalein.

in this case does not show a minimum between the two maxima associated with the two convective regions, but rather an additional maximum unassociated with convection at this time. The vorticity pattern thus has a structure more reminiscent of a long, SE–NW-tilted ITCZ than of a wave train, although the pattern in T_{BB} is not ITCZ-like.

4. Conclusions

We have used KWAJEX soundings and radar data, satellite datasets, and ECMWF analyses to provide a large-scale overview of the meteorology in the tropical western and central North Pacific during the period of KWAJEX (23 July–15 September 1999). We have analyzed the soundings and radar to investigate relationships on daily time scales during this period between rainfall and several variables that have been hypothesized to be agents of thermodynamic control on deep tropical convection. We have identified the primary modes of large-scale variability during this period and

shown how those modes were related to the three largest rain events measured by the Kwajalein ground radar.

Boundary layer moist static energy is strongly correlated with lower-tropospheric (700–960 hPa) mean temperature, but not with upper-tropospheric (600–200 hPa) mean temperature. The relationship between both upper- and lower-tropospheric layer mean RH and area-averaged rain rate is broadly consistent with that seen in other studies. There is a positive relationship with much scatter. High values of lower to midtropospheric RH can coexist with a very low rain rate, but low RH almost never occurs simultaneously with any significant rain. Lag correlations show lower-tropospheric RH leading rain and upper-tropospheric RH lagging it, reinforcing our prior notions that lower-tropospheric moisture exerts some degree of causal control on the occurrence of deep convection while upper-tropospheric moisture is primarily a passive response to deep convection. A related observation from a specific example is that column-integrated water vapor path leads rainfall in the large MRG-influenced rain event of 11 August.

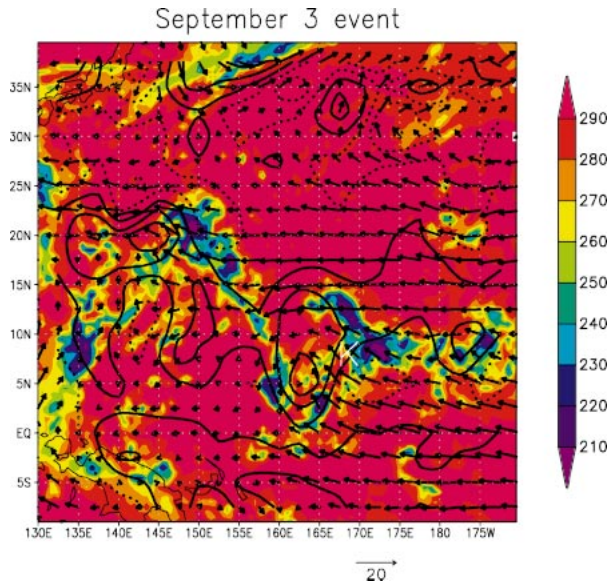


FIG. 17. Synoptic map of GMS IR (0400 UTC) and ECMWF 850-hPa wind and vorticity (1200 UTC) for 3 Sep event; all fields plotted as in Fig. 13.

Pseudoadiabatic, nonentraining CAPE has a weak negative correlation with rain rate. There appears to be little relation of surface wind speed to rain rate, in contrast to the warmest parts of the Pacific ITCZ. There is some indication that this may be due to canceling roles of surface latent heat fluxes and moisture advection associated with zonal wind variations in this region.

The 850-hPa meridional wind field shows the expected westward-propagating synoptic-scale disturbances seen in many previous studies of this region and season. Initial inspection of the GMS IR data suggests much more complexity in that field, and a loose connection between convection and the waves in the winds, in general. However, the three largest rainfall events measured by the ground radar during Kwajalein were associated with disturbances in which both the convection and wind signals propagated coherently within a synoptic-scale envelope.

Spectral filtering shows that convectively coupled equatorial waves, especially mixed Rossby–gravity and Kelvin waves, were important modulators of convection during KWAJEX. Of the three major rain events, a Kelvin wave played a role in the events of 25 July and possibly 11 August, and an MRG wave disturbance was a dominant influence in that of 11 August. The 3 September event was associated with a “TD type” disturbance, or off-equatorial vortex/short Rossby wave packet. The roles of westward-propagating TD-type disturbances and MRG waves have been quite well documented previously. The occurrence of Kelvin waves affecting the region has also been documented (Takayabu and Murakami 1991; Dunkerton and Crum 1995; Wheeler and Kiladis 1999; Straub and Kiladis 2003). Here we show how these different wave types combined

and interacted to modulate the weather during a specific season in the Marshall Islands.

Both MRG and Kelvin waves have eastward group velocity. Short Rossby waves do as well, though their intrinsic group velocity is small so that their total ground-relative group velocity is quite dependent on the mean flow. In the 25 July and 11 August cases, there is an appearance of eastward energy propagation by Rossby wave radiation from tropical cyclones to the northwest of the Marshall Islands. Thus, despite that the mean flow and phase propagation of many synoptic-scale disturbances are from the east, there appear to be times when some of the energy in synoptic scales at Kwajalein comes from the west.

Our focus here on the KWAJEX period derives from the availability of special datasets obtained during the experiments, in particular the soundings, as well as our goal of providing context for other studies of KWAJEX data. Looking closely at specific events also lends concreteness to a general inquiry into the mechanisms influencing precipitation. Future research will broaden this investigation by analyzing data from a longer period. In addition to the routinely available satellite data and operational analyses, research quality Kwajalein radar data are now available continuously from the time of KWAJEX to the present. Increasing our temporal sample should improve our perspective on the role of large-scale waves and their interaction with convection in this region.

Acknowledgments. We thank Larissa Back, Marc Michelsen, and Dan Shaevitz for help processing data, and David Raymond for discussions. We also thank J. M. Fair and G. Trapp of Aeromet Inc. and the students and staff responsible for launching and archiving the upper-air soundings during KWAJEX. GMS data were obtained from the Space Science and Engineering Center at the University of Wisconsin, SSM/I data were obtained from Remote Sensing Systems Inc., and ECMWF data were obtained from the Data Support Section of the National Center for Atmospheric Research. This work was primarily supported by NASA TRMM Grant NAG5-9657. Additionally, SEY acknowledges support from NASA TRMM Grant NAG5-9720, AHS acknowledges support from NASA Grant NAG5-10607, and GNK acknowledges support from the Pan American Climate Studies Program of the NOAA Office of Global Programs under Project GC01-351.

APPENDIX

Sounding Processing and Error Estimation

Soundings were taken during KWAJEX at five sites using three types of sounding systems by personnel with varying levels of training. We uncovered errors involving bad data, incorrect labeling of units (at Kwajalein and Roi-Namur), and incompatibilities between surface

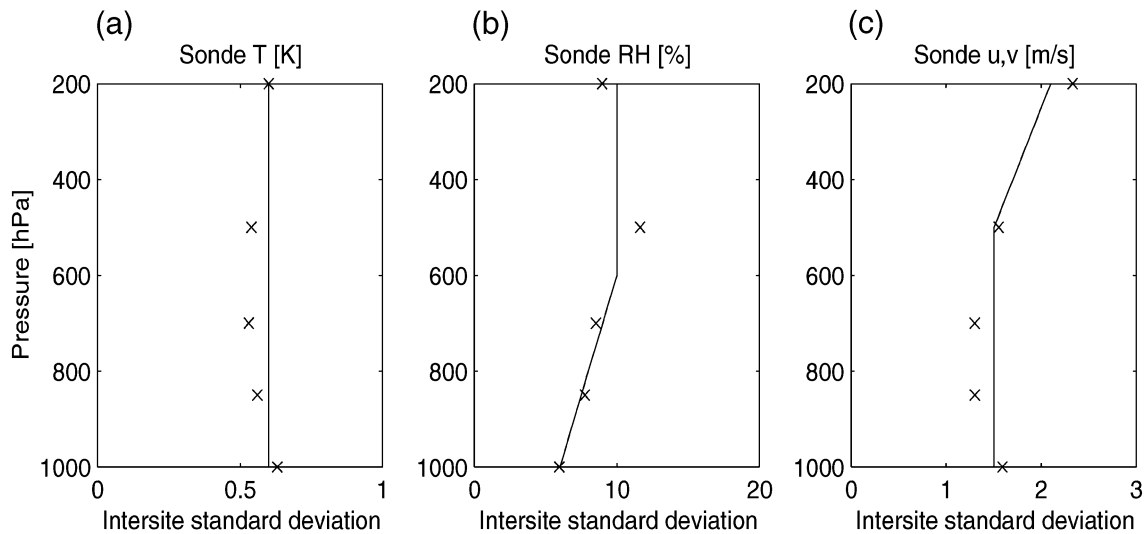


FIG. A1. Estimated single-sounding sampling variability at selected levels (crosses) of (a) temperature, (b) relative humidity, and (c) velocity components. Lines indicate the fit curves of (A1).

and radiosonde measurements (at Lae and Woja). However, once these errors have been removed there is a reassuringly high level of spatial and temporal compatibility between the soundings, allowing reliable detection of synoptic variability in all measured variables. We first describe our quality control procedure, then estimate the random sampling variability between coincident measurements at the different sites, and in daily mean array averages of these measurements.

The starting point for the quality control procedure was the raw upper-air sounding data recorded in the field. For Roi-Namur and Kwajalein soundings this consisted of the 2-s data with a corresponding pressure difference between levels of approximately 1 hPa. For the *Ronald H. Brown* soundings, the raw data contains values every 10 s corresponding to pressure differences of approximately 3 hPa between levels. For the Lae and Woja soundings, the recorded files contain data every 5 hPa.

a. Quality control procedures

The quality control procedure consisted of the following steps:

- 1) We removed gross errors in basic measured variables T , RH, and wind speed and direction by testing if each basic variable at each level in the raw data files was in a broad allowable range, and setting it to missing if it was not.
- 2) In the raw data, if the upward gradient between consecutive pressure levels in any variable exceeded a specified threshold, that variable was set to missing at all overlying pressure levels. This check was designed to remove data compromised by icing of sensors and primarily impacted relative humidity and dewpoint (particularly at Lae and Woja), but also caught occasional temperature errors.
- 3) At any given level, if one of several related variables failed the above tests and had been set to missing, all the related variables at that level were also set to missing. For instance, if RH was missing, then dewpoint would also be set to missing. Similarly, if wind direction were missing, wind speed, u , and v would be set to missing.
- 4) If after the above tests, less than 5% of the wind data remained valid, then all winds in a particular sounding were set to missing. This test primarily affected wind data obtained by the *Ronald H. Brown*, which experienced sonde tracking problems more frequently than the other sites.
- 5) Layer-average values were computed for 25-hPa layers centered on 850 hPa to 75 hPa and for 10-hPa layers centered on 860 hPa to 1000 hPa yielding a simplified sounding with 48 pressure levels. Derived parameters u and v were computed from measured wind speed and wind direction. The surface data were not used in the averaging due to possible incompatibilities with the rest of the sounding.
- 6) Surface data were only subjected to limit checks (no gradient checks) and a check to see if all surface variables were present in a given sounding. If all variables were not present, operator error was assumed and all surface variables were set to missing. Because surface data were obtained from a different measurement system than the soundings and may contain sizable errors not detected by the above checks, caution is advised in using them even after our quality control checks.
- 7) We found by comparing wind speed at different

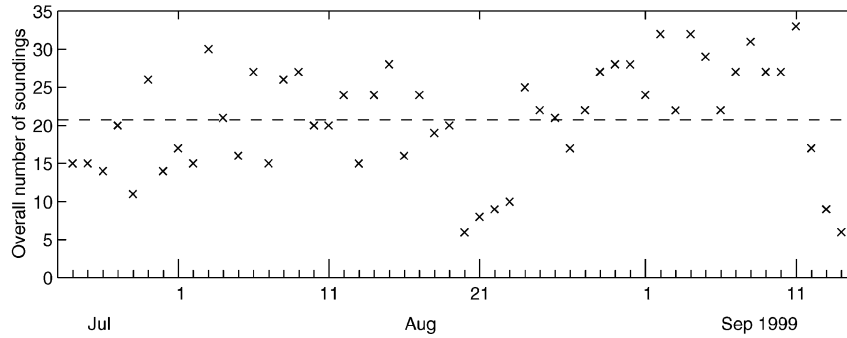


FIG. A2. Daily frequency of all sonde launches at the five sites of the KWAJEX array. The dashed line shows the KWAJEX time-mean frequency.

sites that Kwajalein and Roi-Namur usually (but not always) recorded wind speeds in meters per second even though the stated unit in their data file headers was knots. To determine the correct wind speed units in any sounding at either of these locations, its wind speed averaged over all levels between 900 and 600 hPa with nonmissing data was compared with a 24-h running-mean wind speed averaged over the same pressure levels, composited using the remaining three stations (the *Ronald H. Brown*, Lae, and Woja; or BLW). For instance, for a Kwajalein sounding at a nominal time of 0300 UTC on 28 July with valid wind speeds only from 800 to 500 hPa, we would compute its 800–600-hPa averaged wind speed W_K . We would also compute the 800–600-hPa averaged wind speed W_{BLW} based on a time mean of all available soundings from BLW starting 12 h before (1500 UTC 27 July) to 9 h after (1200 UTC 28 July). We then computed the wind speed ratio $R_{BLW} = W_K/W_{BLW}$. In practice, values of R_{BLW} tended to cluster around 0.52 (indicating a units conversion error, since 1 kt = 0.52 m s⁻¹). However, in about 10% of the soundings R_{BLW} was close to 1, indicating no such error. If $R_{BLW} < 0.75$, we divided all wind speeds in the individual Kwajalein or Roi-Namur sounding by 0.52, and recomputed the vector wind components accordingly.

- 8) We sorted soundings into 3-h blocks around nominal times of 0000, 0300, . . . , 2100 UTC. Each block included soundings launched between 2 h before and 1 h after the nominal time.
- 9) We computed preliminary time-mean and perturbation soundings for each site, and array averaged across all sites. From the array-averaged perturbation soundings, we calculated vertical profiles of the average deviation (the time mean of the absolute value of the array-averaged perturbation) of each variable.
- 10) At each site and time, we examined the perturbation sounding of each variable to look for outliers. If at any pressure level, the perturbation exceeded four

- times the average deviation of that variable at that level, that variable was set to missing at that level.
- 11) We recomputed the time-mean and perturbation soundings for each site and the array mean.

b. Estimation of typical intersite variability

For all times when soundings were launched at multiple sites, we calculated the differences in the perturbations of each variable at each site from their array-averaged values. We used this to estimate the standard deviation of the perturbation between the reporting sites at that time. We then time averaged all of these standard deviation estimates to get an estimate of typical intersite variability. This was done separately for several representative pressure levels. Figure A1 shows the estimated standard deviation σ_1 for T , RH, u , and v . A combined plot is shown for the velocity components, since the standard deviations for the two velocity components exhibited very similar behavior. The magnitude and vertical structure of variability in each variable are similar to those found by Mapes et al. (2003) using data obtained from sounding arrays in two other tropical field experiments. The fitting curves shown in the figure (with pressure p in hPa) are

$$\sigma_1(T) = 0.6 \text{ K},$$

$$\sigma_1(\text{RH}) = 0.1 - 0.01 \max(p - 600, 0), \quad \text{and}$$

$$\sigma_1(u, v) = 1.5 + 0.002 \max(500 - p, 0) \text{ m s}^{-1}. \quad (\text{A1})$$

We also looked at pairs of soundings at the same site separated in time. The typical differences between soundings taken within 6 h of each other were comparable to the above intersite variability, suggesting that binning the soundings into 6-h blocks is a good way to reduce the sampling uncertainty while preserving the underlying synoptic variability.

In this paper, we have gone further and binned the soundings into daily mean array averages. To estimate the sampling uncertainty of such mean soundings, we need to divide σ_1 by the square root of the number of

soundings N_d taken in the full array on a typical day. A time series of this quantity during KWAJEX is shown in Fig. A2. Some periods were more densely sampled than others, but choosing a representative value $N_d = 20$ we conclude that as a rough guideline, the random sampling errors in daily mean array-average (daa) quantities are

$$\begin{aligned}\sigma_{\text{daa}}(T) &\approx 0.15 \text{ K}, \\ \sigma_{\text{daa}}(\text{RH}) &\approx 0.02, \quad \text{and} \\ \sigma_{\text{daa}}(u, v) &\approx 0.4 \text{ m s}^{-1},\end{aligned}\quad (\text{A2})$$

with some minor variation between pressure levels. These are quite small compared to the day-to-day variability in all of these quantities. This suggests that we can accurately track synoptic-scale variations over the KWAJEX region using the daily array-average perturbation soundings.

REFERENCES

- Arakawa, A., and W. H. Schubert, 1974: Interaction of a cumulus cloud ensemble with the large-scale environment, Part I. *J. Atmos. Sci.*, **31**, 674–701.
- Betts, A. K., and M. J. Miller, 1986: A new convective adjustment scheme. Part II: Single column tests using GATE wave, BOMEX, ATEX, and arctic air-mass data jets. *Quart. J. Roy. Meteor. Soc.*, **112**, 693–709.
- Brown, R. G., and C. S. Bretherton, 1997: A test of the strict quasi-equilibrium theory on long space and time scales. *J. Atmos. Sci.*, **54**, 624–638.
- , and C. Zhang, 1997: Variability of midtropospheric moisture and its effect on cloud-top height distribution during TOGA COARE. *J. Atmos. Sci.*, **54**, 2760–2774.
- Chang, C.-P., J. M. Chen, P. A. Harr, and L. E. Carr, 1996: Northwestward-propagating wave patterns over the tropical western North Pacific during summer. *Mon. Wea. Rev.*, **124**, 2245–2266.
- Chen, S. S., R. A. Houze Jr., and B. E. Mapes, 1996: Multiscale variability of deep convection in relation to large-scale circulation in TOGA COARE. *J. Atmos. Sci.*, **53**, 1380–1409.
- Davidson, N. E., and H. H. Hendon, 1989: Downstream development in the Southern Hemisphere monsoon during FGGE/WMONEX. *Mon. Wea. Rev.*, **117**, 1458–1470.
- Dickinson, M. J., and J. Molinari, 2002: Mixed Rossby–gravity waves and western Pacific tropical cyclogenesis. Part I: Synoptic evolution. *J. Atmos. Sci.*, **59**, 2183–2196.
- Dunkerton, T. J., and M. P. Baldwin, 1995: Observation of 3–6-day meridional wind oscillations over the tropical Pacific, 1973–1992: Horizontal structure and propagation. *J. Atmos. Sci.*, **52**, 1585–1601.
- , and F. X. Crum, 1995: Eastward propagating 2- to 15-day equatorial convection and its relation to the tropical intraseasonal oscillation. *J. Geophys. Res.*, **100**, 25 781–25 790.
- Emanuel, K. A., 1995: The behavior of a simple hurricane model using a convective scheme based on subcloud-layer entropy equilibrium. *J. Atmos. Sci.*, **52**, 3960–3968.
- , J. D. Neelin, and C. S. Bretherton, 1994: On large-scale circulations in convecting atmospheres. *Quart. J. Roy. Meteor. Soc.*, **120**, 1111–1143.
- Flierl, G. R., M. E. Stern, and J. A. Whitehead Jr., 1983: The physical significance of modons: Laboratory experiments and general integral constraints. *Dyn. Atmos. Oceans*, **7**, 233–263.
- Holland, G. J., 1995: Scale interaction in the western Pacific monsoon. *Meteor. Atmos. Phys.*, **56**, 57–79.
- Holton, J. R., 1971: A diagnostic model for equatorial wave disturbances: The role of vertical shear of the mean zonal wind. *J. Atmos. Sci.*, **28**, 55–64.
- Kiladis, G. N., and K. M. Weickmann, 1997: Horizontal structure and seasonality of large-scale circulations associated with sub-monthly tropical convection. *Mon. Wea. Rev.*, **125**, 1997–2013.
- Kingsmill, D. E., and R. A. Houze Jr., 1999: Thermodynamic characteristics of air flowing into and out of precipitating convection over the west Pacific warm pool. *Quart. J. Roy. Meteor. Soc.*, **125**, 1209–1229.
- Kummerow, C., and Coauthors, 2000: The status of the Tropical Rainfall Measuring Mission (TRMM) after two years in orbit. *J. Appl. Meteor.*, **39**, 1965–1982.
- Lau, K.-H., and N.-C. Lau, 1990: Observed structure and propagation characteristics of tropical summertime synoptic scale disturbances. *Mon. Wea. Rev.*, **118**, 1888–1913.
- Liebmann, B., and H. H. Hendon, 1990: Synoptic-scale disturbances near the equator. *J. Atmos. Sci.*, **47**, 1463–1479.
- Lucas, C., and E. J. Zipser, 2000: Environmental variability during TOGA COARE. *J. Atmos. Sci.*, **57**, 2333–2350.
- Mapes, B. E., and R. A. Houze Jr., 1992: An integrated view of the 1987 Australian monsoon and its mesoscale convective systems. Part I: Horizontal structure. *Quart. J. Roy. Meteor. Soc.*, **118**, 927–963.
- , P. E. Ciesielski, and R. H. Johnson, 2003: Sampling errors in rawinsonde-array budgets. *J. Atmos. Sci.*, **60**, 2697–2714.
- McPherson, T., and W. Stapler, 2000: 1999 annual tropical cyclone report. U.S. Naval Pacific Meteorology and Oceanography Center/Joint Typhoon Warning Center, Pearl Harbor, HI, 213 pp.
- McWilliams, J. C., P. R. Gent, and N. J. Norton, 1986: The evolution of balanced, low-mode vortices on the β -plane. *J. Phys. Oceanogr.*, **16**, 838–855.
- Murakami, T., and J. Matsumoto, 1994: Summer monsoon over the Asian continent and western North Pacific. *J. Meteor. Soc. Japan*, **72**, 719–745.
- Neelin, J. D., and I. M. Held, 1987: Modeling tropical convergence based on the moist static energy budget. *Mon. Wea. Rev.*, **115**, 3–12.
- Nitta, T., and Y. Takayabu, 1985: Global analysis of the lower tropospheric disturbances in the Tropics during the northern summer of the FGGE year. Part II: Regional characteristics of the disturbances. *Pure Appl. Geophys.*, **123**, 272–292.
- Petersen, W. A., R. Cifelli, D. J. Boccippio, S. A. Rutledge, and C. Fairall, 2003: Convection and easterly wave structures observed in the eastern Pacific warm pool during EPIC-2001. *J. Atmos. Sci.*, **60**, 1754–1773.
- Raymond, D. J., 1995: Regulation of moist convection over the west Pacific warm pool. *J. Atmos. Sci.*, **52**, 3945–3959.
- , 2000: The thermodynamic control of tropical rainfall. *Quart. J. Roy. Meteor. Soc.*, **126**, 889–898.
- , G. B. Raga, C. S. Bretherton, J. Molinari, C. Lopéz-Carillo, and Ž. Fuchs, 2003: Convective forcing in the intertropical convergence zone of the eastern Pacific. *J. Atmos. Sci.*, **60**, 2064–2082.
- Reed, R. J., and E. E. Recker, 1971: Structure and properties of synoptic-scale wave disturbances in the equatorial western Pacific. *J. Atmos. Sci.*, **28**, 1117–1133.
- Schumacher, C., and R. A. Houze Jr., 2000: Comparison of radar data from the TRMM satellite and Kwajalein oceanic validation site. *J. Appl. Meteor.*, **39**, 2151–2164.
- Serra, Y. L., and R. A. Houze Jr., 2002: Observations of variability on synoptic timescales in the east Pacific ITCZ. *J. Atmos. Sci.*, **59**, 1723–1743.
- Sherwood, S. C., 1999: Convective precursors and predictability in the tropical western Pacific. *Mon. Wea. Rev.*, **127**, 2977–2991.
- , and R. Wahrlich, 1999: Observed evolution of tropical deep convective events and their environment. *Mon. Wea. Rev.*, **127**, 1777–1795.
- Sobel, A. H., and C. S. Bretherton, 1999: Development of synoptic-scale disturbances over the summertime tropical northwest Pacific. *J. Atmos. Sci.*, **56**, 3106–3127.

- , and T. Horinouchi, 2000: On the dynamics of easterly waves, monsoon depressions, and tropical depression type disturbances. *J. Meteor. Soc. Japan*, **78**, 167–173.
- , and C. S. Bretherton, 2003: Large-scale waves interacting with deep convection in idealized mesoscale model simulations. *Tellus*, **55A**, 45–60.
- Straub, K. H., and G. N. Kiladis, 2002: Observations of a convectively coupled Kelvin wave in the eastern Pacific ITCZ. *J. Atmos. Sci.*, **59**, 30–53.
- , and —, 2003: The observed structure of convectively coupled Kelvin waves: Comparison with simple models of coupled wave instability. *J. Atmos. Sci.*, **60**, 1655–1668.
- Takayabu, Y. N., and M. Murakami, 1991: The structure of super cloud clusters observed in 1–20 June 1986 and their relationship to easterly waves. *J. Meteor. Soc. Japan*, **69**, 105–125.
- , and T. Nitta, 1993: 3–5 day period disturbances coupled with convection over the tropical Pacific Ocean. *J. Meteor. Soc. Japan*, **71**, 221–246.
- Thompson, R. M., S. W. Payne, E. E. Recker, and R. J. Reed, 1979: Structure and properties of synoptic-scale wave disturbances in the intertropical convergence zone of the eastern Atlantic. *J. Atmos. Sci.*, **36**, 53–72.
- Tompkins, A. M., 2001: Organization of tropical convection in low vertical wind shears: The role of water vapor. *J. Atmos. Sci.*, **58**, 529–545.
- Wallace, J. M., and C.-P. Chang, 1969: Spectrum analysis of large-scale wave disturbances in the tropical lower troposphere. *J. Atmos. Sci.*, **26**, 1010–1025.
- Wheeler, M., and G. N. Kiladis, 1999: Convectively coupled equatorial waves: Analysis of clouds and temperature in the wave-number–frequency domain. *J. Atmos. Sci.*, **56**, 374–399.
- , —, and P. J. Webster, 2000: Large-scale dynamical fields associated with convectively coupled equatorial waves. *J. Atmos. Sci.*, **57**, 613–640.
- Wang, B., R. Wu, and K.-M. Lau, 2001: Interannual variability of the Asian summer monsoon: Contrasts between the Indian and the western North Pacific–east Asian monsoons. *J. Climate*, **14**, 4073–4090.